Estuarine, Coastal and Shelf Science 297 (2024) 108618

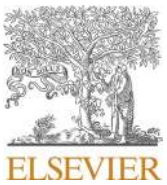

Contents lists available at ScienceDirect

Estuarine, Coastal and Shelf Science

journal homepage: www.elsevier.com/locate/ecss

River–coastal–ocean continuum modeling along the Lazio coast (Tyrrhenian Sea, Italy): Assessment of near river dynamics in the Tiber delta

Simone Bonamano [a,b], Ivan Federico [b,*], Salvatore Causio [b], Viviana Piermattei [a,b], Daniele Piazzolla [b], Sergio Scanu [b], Alice Madonia [b], Nicola Madonia [a], Giovanni De Cillis [b], Eric Jansen [b], Giorgio Fersini [c], Giovanni Coppini [b], Marco Marcelli [a]

[a] Laboratory of Experimental Oceanology and Marine Ecology, DEB, Tuscia University, Molo Vespucci, Port of Civitavecchia, 00053, Civitavecchia, RM, Italy
[b] Centro Euro-Mediterraneo Sui Cambiamenti Climatici – Ocean Predictions and Applications, via Marco Biagi 5, 73100, Lecce, Italy
[c] Port System Authority of the Central Northern Tyrrhenian Sea, Molo Vespucci, Port of Civitavecchia, 00053, Civitavecchia, RM, Italy

ARTICLE INFO

Keywords:
Numerical models
Unstructured-grid modeling
Near-shore dynamics
Estuarine dynamics
Tiber river
Oceanographic observations
Anticyclonic gyre

ABSTRACT

The complex processes that occur in river delta areas cannot be fully resolved using traditional structured-mesh models. A seamless unstructured-grid approach could support advances in the estimation and modeling of such dynamics across scales. In this paper, a river–coastal–ocean continuum modeling representation was developed for the Tiber River delta, including surrounding coastal areas and open-ocean zones along the Lazio coast (Tyrrhenian Sea, Italy). Using temperature and salinity profiles acquired from historical data of near-river CTD, we demonstrate that this representation reproduces the coastal dynamic processes in the Tiber delta zone better than the classic coastal–ocean representation, minimizing the need for calibration and sensitivity experiments. The model results are compared to a large amount of new observational data (temperature, salinity, and surface currents) obtained specifically to investigate multiple spatial and temporal processes (open-ocean, coastal and near- and along-river). In general, the model shows good overall accuracy, also in reproducing salt wedge intrusion along the southern Tiber branch. Moreover, the results suggest the presence of an anticyclonic gyre in the vicinity of the river mouth of the northern branch that is induced mainly by river discharge and coastal morphology. Owing to its capacity to simulate multi-scale processes in a seamless fashion from the open ocean to the river delta zone, this model can be implemented in the near future within an operational framework to support coastal forecasting activities and deliver useful and reliable ocean information.

1. Introduction

River deltas are complex areas where extremely dynamic processes occur that require a holistic multi- or cross-scale modeling approach in which all hydrodynamic fields are considered integral parts of the overall environment (Jickells et al., 2016).

The interaction between riverine freshwater and ambient saltwater has been studied by means of shallow water and primitive equation models under both idealized and realistic conditions (Kourafalou et al., 1996a, 1996b; Ferrarin et al., 2019; Maicu et al., 2018, 2021). These studies have shown that the dynamic scales of motion involved in the problem range from local scales, i.e., a few tens of meters to several kilometers, to scales of more than 100 km, where persistent mesoscale features such as gyres and jets embed the riverine plume in a complex, large-scale structure with a typical meandering jet flowing along or at some distance from the coast (Inghilesi et al., 2012).

Given the complexity of this transitional environment and its extremely dynamic processes (e.g., freshwater effects in denser water, two-layer flows, mixing processes) characterized by compounding effects among multiple characteristics (e.g., river width and slope, wind regimes at the land–ocean interface, processes on the continental shelves), comprehensive studies which integrated different sources of information (in-situ surveys, innovative platforms/sensors, remote sensing technique and numerical simulations) are necessary (Sorgente et al., 2020; Baldoni et al., 2022; Postacchini et al., 2023).

Notably, numerical simulations of water circulation and the

* Corresponding author.
E-mail address: ivan.federico@cmcc.it (I. Federico).

https://doi.org/10.1016/j.ecss.2024.108618
Received 30 January 2023; Received in revised form 22 December 2023; Accepted 4 January 2024
Available online 5 January 2024

principal physical processes affecting coastal areas interested by river discharge require the use of both three-dimensional (3D), cross-scale, high-resolution, fully baroclinic models and downscaling techniques capable of reproducing mass exchange processes between the coastal area and the open sea (Ferrarin et al., 2019; Federico et al., 2017).

This goal can be achieved through the implementation of numerical models based on a unique unstructured grid capable of describing processes at multiple spatial scales (Cucco et al., 2012; Ferrarin et al., 2016; Federico et al., 2017; Stanev et al., 2017). This approach overcomes the shortcomings of previous studies based on numerical methods in coastal areas affected by river discharge, which were limited to one or several components of the macrosystem and lacked an integrated and comprehensive approach (Rasmussen et al., 2009; Cerralbo et al., 2014; El-Adawy et al., 2014; Bonamano et al., 2021).

In addition to the application of an appropriate seamless cross-scale model and adequately fine resolution, gaps in observations in coastal, near-river, and along-river areas (Kourafalou et al., 2015b; Wilkin et al., 2017) must be addressed, requiring effort for the collection of synoptic and distributed observational data. This requirement is fundamental to model calibration and validation as well as the planning of possible data assimilation strategies for future application.

The main objective of this paper is linking these two components: an accurate river–coastal–ocean continuum modeling representation and a massive collection of data newly acquired for the purpose of model verification.

The area of interest includes the Tiber River and the surrounding coastal and open-ocean zones along the Lazio coast of the Tyrrhenian Sea (Western Mediterranean Sea) (see Fig. 1).

The Tiber River basin represents a particular challenge, as it is a coastal region that is strongly affected by air–sea, land–sea, and coastal–offshore interactions.

The Tiber River is 409 km in length and originates in the Italian region of Emilia Romagna at about 1268 m a.s.l. Its basin covers 1.79 × 10^4 km^2 across the Italian regions of Emilia Romagna, Tuscany, Umbria, and Lazio. After crossing through the urban area of Rome (La Vigna et al., 2010), it flows into the Tyrrhenian Sea, forming an estuary with two branches divided by a small island (Fig. 1). The Tiber River has variable discharge, increasing in the period of October to June and decreasing from July to September (Manca et al., 2014). The northern branch receives approximately 20% of the total Tiber River flow (Mikhailova et al.,1999). Being in the microtidal environments category (Davies, 1964), the coastal zones near the Tiber River are characterized by small tidal currents and limited tidal range less than 0.2 m (Inghilesi et al., 2012). The outflow of this river impacts the open-ocean circulation of the Tyrrhenian Sea at the subregional scale, with a strong coastal jet driven by intense flood events during the winter season and a sea breeze regime in the summer that can shift the river plume toward the offshore area and trigger local coastal upwelling (Inghilesi et al., 2012).

To date, the Tiber River delta zone has been investigated using numerical models and satellite observations (Inghilesi et al., 2012; Pitarch et al., 2019), as well as *in situ* measurements collected within the river branches (Manca et al., 2014). However, no studies have yet attempted to investigate the dynamics of the Tiber river-coastal-ocean continuum. Specifically, the numerical models developed in this area allow for an analysis of the transport of conservative substances, particularly sediments, employing both Lagrangian (Inghilesi et al., 2012) and Eulerian (Pitarch et al., 2019) approaches. Inghilesi et al. (2012) employed a 3D model (POM) implementation at the subregional scale covering the entire Tyrrhenian Sea basin. This model featured 26 sigma layers and maintained a constant horizontal spatial resolution of approximately 2 km throughout the computation domain. Pitarch et al. (2019) developed a very limited-area modelling implementation with DELFT3D model based on curvilinear finite difference grid with square elements of 30 × 30 m, confined in a computation domain of 3 km × 3 km centered around the Tiber River mouth.

In this study, we assessed the benefit of using a river–coastal–ocean continuum representation rather than a classical coastal–ocean representation that excludes the river branches and consider inputs on the basis of multiple factors that can be calibrated (e.g., partitioning of discharge between the branches and salinity set as a lateral boundary condition at the ocean-river interface). We also evaluated model performance at multiple scales with observational data (from a conductivity–temperature–depth [CTD] instrument, drifter, and X-band radar) newly acquired for this work to validate multiple parameters (active tracers and sea velocities). Finally, we used the model to reproduce salt wedge intrusion along the southern river branch and to assess specific local dynamics, such as the formation of an anticyclonic gyre in the near-river and coastal zone, as well as to identify the main drivers of these processes.

The remainder of this paper is organized as follows. Section 2 describes the observational dataset, with a specific focus on the newly acquired data. Section 3 presents the modeling system along with the numerical set-up and forcings, including the main outcomes related to coastal–ocean vs. river–coastal–ocean representation. In Section 4, accurate validation at multiple spatial scales is detailed, including the processes used to investigate salt wedge intrusion. River-induced gyre formation and their main drivers are presented in Section 5. Conclusions

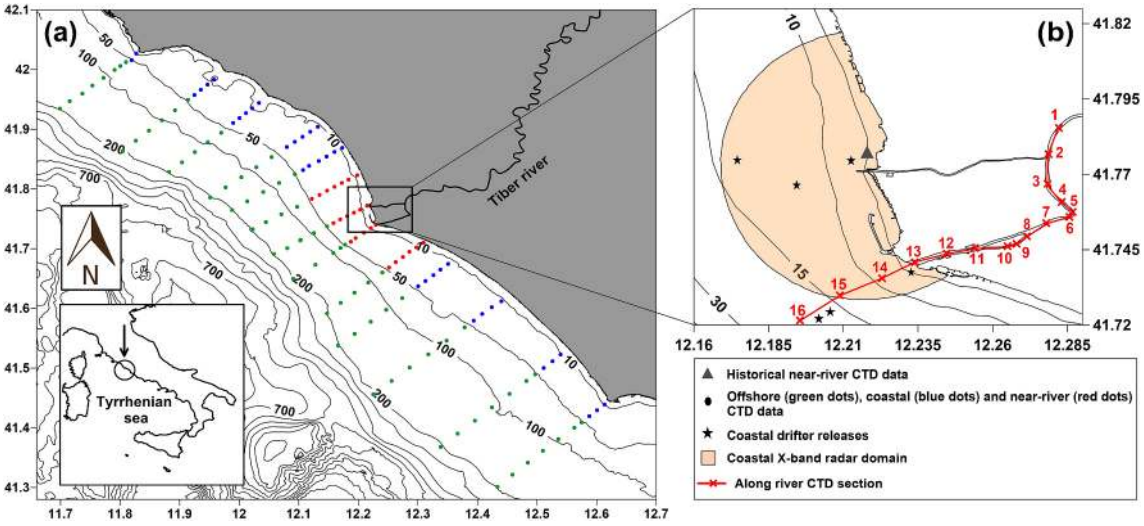

Fig. 1. Coastline and bathymetry of the study area. All observational datasets, both historical and newly acquired, used for validation are reported in the maps.

and future perspectives are provided in Section 6.

2. Observational dataset

In coastal areas, *in situ* and remote sensing observations are essential for the analysis and forecasting of specific events (Schofield et al., 2002) and to support coastal management related to detection of conflicts between anthropic pressures and sensitive areas (Bonamano et al., 2016).

The observations used for model validation can be summarized as historical datasets and datasets newly acquired for this paper.

Among historical datasets, sea surface temperature (SST) data collected using infrared sensors mounted on various satellite platforms at ultra-high spatial resolution (UHR, 0.01°), distributed by the Copernicus Marine Service (CMS) as observational products (Buongiorno Nardelli et al., 2013), were used to analyze the annual variability in SST in 2018 and 2019.

Furthermore, historical near-river CTD data were used specifically for the calibration of the river–coastal–ocean continuum model in the coastal–ocean configuration. This dataset consists of 31 temperature and salinity profiles in the northern Tiber branch acquired during the summer.

Here we describe the newly acquired observational data at multiple scales (offshore, coastal, near-river, along-river), which is applied in Section 4.

- **Offshore, coastal and near-river CTD data.** The temperature and salinity of the water column were measured between August and November 2020 along 13 cross-shore sections (136 casts) with maximum depths ranging from 10 m to 200 m to analyze the interactions between the river plume and offshore processes. As shown in Fig. 1a, the vertical profiles were grouped into near-river (red dots), coastal (blue dots) and offshore (black dots), on the basis of the physical characteristics of the water masses (e.g., T/S diagrams). For both surveys, the Idronaut Ocean Seven 316 Multi-Parameter Probe (Piermattei et al., 2018; Martellucci et al., 2021) was used.
- **Coastal X-band radar.** The surface velocity field in the coastal zone of the Tiber River was investigated with X-band radar installed at the mouth of the northern branch of the Tiber River in December 2020, on a 10 m high light tower located at 41.7706°N and 012.2210°E. These observations allow for detection of the surface velocity field through statistical processing of the electromagnetic response backscatter signal re-emitted by the surface of the sea, representing roughness associated with Bragg resonance (Serafino et al., 2010).
- **Coastal drifters.** Surface sea currents were analyzed through the release of six coastal drifters at sites corresponding to the two river mouths, with three released in the southern branch and three in the northern branch. Specifically, four Coastal Nomad Drifter buoys (SouthTEK Sensing Technologies), designated NOMAD (Ribotti et al., 2022), and two low-cost Lagrangian coastal buoys, referred to as MONSTER (Marcelli et al., 2021) (developed by the Laboratory of Experimental Oceanology and Marine Ecology), were launched on February 17 and March 3, 2021, and remained in the sea for about 8 h. Both types of drifters were equipped with a GPRS/GSM data transmission system that sent position data every 5min.
- **Along-river data.** Processes at the river–sea interface were investigated along the southern branch of the Tiber River through a one-day survey (on May 15, 2022, between 9 a.m. and 1 p.m.) of16 stations (red line with crosses in Fig. 1b) located along the ocean–river section. Selection of measurement locations was conducted based on the positions illustrated in other previous works (Capelli et al., 2007; Manca et al., 2014). Thermohaline observations within the river branch (13 stations) were collected using a cost-effective CTD probe produced by the Laboratory of Experimental Oceanology and Marine Ecology, while the open-ocean stations (three casts) were sampled with an SBE 911plus probe (Marcelli et al., 2005; Schroeder et al., 2006). Furthermore, the bathymetry of the southern river branch was reconstructed using high-resolution single-beam (EA 400 single beam echosounder; Kongsberg Maritime) data collected from 13 river cross-sections corresponding to the CTD stations. The bathymetric results are shown in Fig. 2*a*.

3. Modeling system

The modeling system used in this study is based on the System of HydrodYnamic Finite Element Modules (SHYFEM), which is a 3D baroclinic finite-element hydrodynamic model (Umgiesser et al., 2004) that solves the Navier–Stokes equations by applying the hydrostatic and Boussinesq approximations. The SHYFEM-MPI version developed by Centro Euro-Mediterraneo sui Cambiamenti Climatici (CMCC) (Micaletto et al., 2022) was used in this study. The unstructured grid is Arakawa B with triangular mesh, which provides accurate representation of irregular coastal boundaries. The peculiarity of unstructured grids is the capacity to represent several scales in a seamless fashion, reaching higher resolution where necessary.

The model uses a semi-implicit algorithm for integration over time (Casulli and Cattani, 1994), which has the advantage of being unconditionally stable with respect to gravity waves, bottom friction, and Coriolis terms, and therefore allows transport variables to be solved explicitly. The Coriolis term and pressure gradient in the momentum equation and the divergence terms in the continuity equation are treated semi-implicitly. Bottom friction and vertical eddy viscosity are treated fully implicitly for stability reasons, while the remaining terms (advective and horizontal diffusion terms in the momentum equation) are treated explicitly. More detailed descriptions of the model equations and discretization methods are provided in Maicu et al. (2021) and Micaletto et al. (2022).

The SHYFEM model has been successfully applied to simulate the hydrodynamics of several systems in the coastal sea and estuaries (e.g., the Po River in Italy, by Ferrarin et al.2019, Maicu et al.2018, 2021; Alessandri et al.2023; and the Savannah River in Georgia, USA, by Park et al.2022).

The modeling approach used here is based on the downscaling of the regional CMS product for the Mediterranean Sea (Med-PHY NRT) (Clementi et al., 2019). The current Med-PHY NRT implementation is based on Nucleus for European Modelling of the Ocean (NEMO), Madec (2008), finite-difference code with a horizontal resolution of 1/24° (approximately 4–5 km), and 141 unevenly spaced vertical levels. The system is supported by a data assimilation system based on the OceanVar scheme (Dobricic and Pinardi, 2008; Storto et al., 2016).

For the solute transport and diffusion equation, the horizontal and vertical advection-dispersion processes are solved with a second order explicit scheme based on the total variance diminishing (TVD) scheme (Darwish and Moukalled, 2003). This approach is complemented by the inclusion of the superbee limiter, which contributes to the effective conservation of the two-layer system, maintaining a distinct interface between the plume and the quiescent layer (Fofonova et al., 2021). This numerical system should enable the accurate replication of the baroclinic currents, buoyant freshwater fluxes, and the sharp horizontal and vertical salinity and density gradients (Maicu et al., 2018).

Horizontal eddy viscosity is determined using Smagorinsky (1963) formulation, while vertical viscosities and diffusivities are calculated with a k-ε scheme adapted from the General Ocean Turbulence Model (GOTM) (Burchard and Petersen, 1999). Bottom stress is computed using the quadratic formulation with a bottom drag coefficient defined based on the logarithmic formulation and water depth. In the logarithmic formulation, the Van Karman constant is assigned a value of 0.4 and the roughness length is 0.01 m (Ferrarin et al., 2019). In this work, all other model parameters are assigned based on previous studies that successfully applied the SHYFEM model in coastal and inland regions (Federico et al., 2017; Trotta et al., 2021; Park et al., 2022).

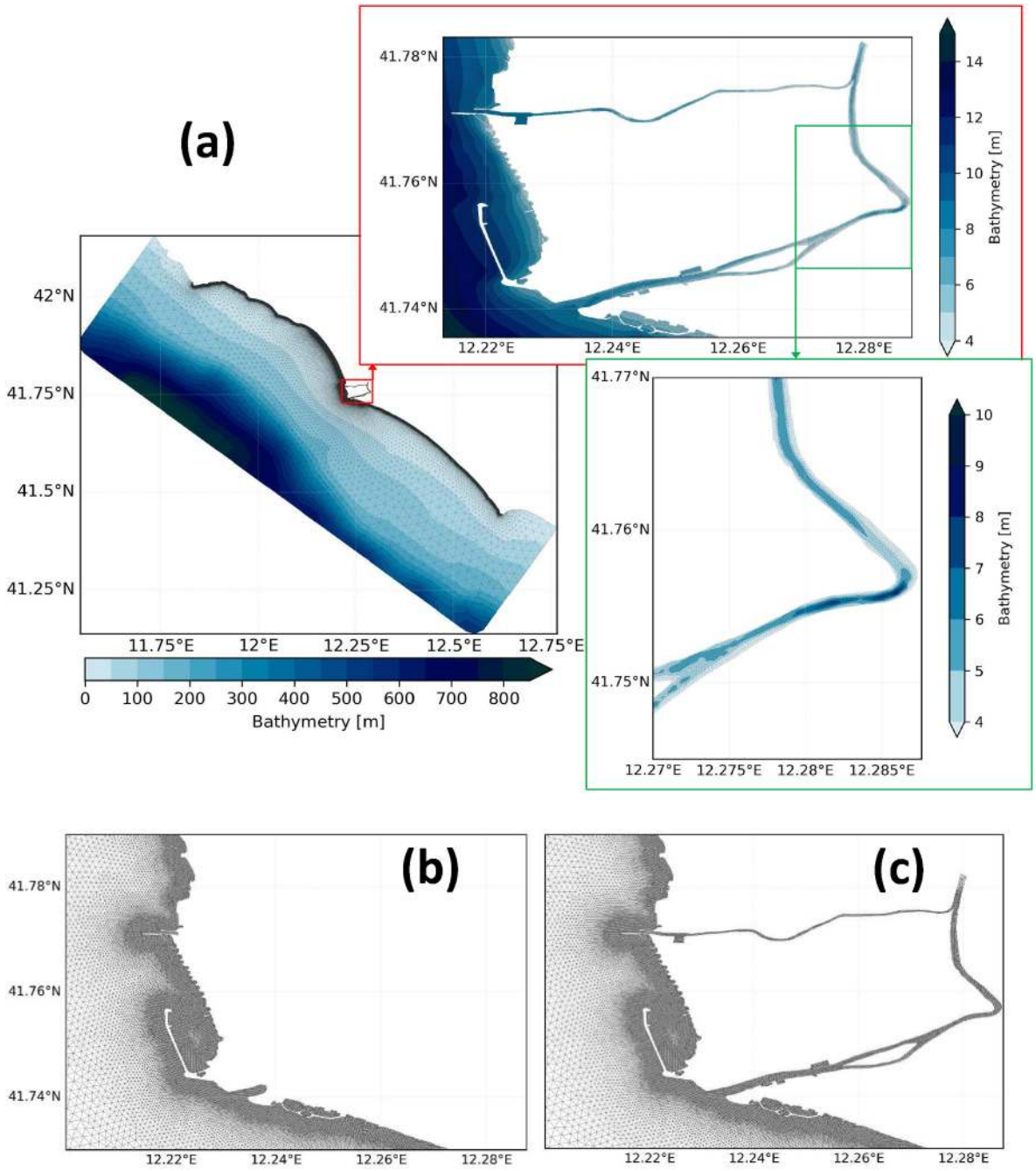

Fig. 2. Horizontal unstructured grid and bathymetry, with the Tiber River branches magnified (*a*). Details of the high-resolution horizontal grids used with the coastal–ocean (CO) (*b*) and river–coastal–ocean (RCO) (*c*) configurations.

3.1. Numerical set-up

The model domain (Fig. 2*a*) extends along approximately 200 km of coast in the northeastern Tyrrhenian Sea, with the Tiber River delta located at the center. The coastline was reconstructed through integration of data extracted from high-resolution satellite images with the Open Street Map dataset (www.openstreetmap.org). The horizontal mesh is created by using advanced and customized meshing tools, allowing higher grid resolution as distance from the coastline for the ocean part of the domain. In the river branches the resolution is almost uniform and no significant anisotropies are present also due to high density of node/elements across the river sections. The tools are based on the GMSH (https://gmsh.info/) for meshing generation and BLENDER (https://www.blender.org/) for optimization and quality check of triangles. The meshing algorithm is a frontal Delaunay approach (Remacle et al., 2013) and the nominal size of the grid refers to the max edge length of the triangle. In coastal waters, the model has the highest spatial resolution, generally reaching an element size of 50 or 100 m, with further refinement in specific areas (e.g., the Tiber River delta and within river branches, Fig. 2*b*) where the resolution reaches 10–20 m. In open-ocean areas, the horizontal resolution is approximately 1–2 km.

The bathymetry was derived from the EMODNET (https://www.emodnet-bathymetry.eu/) product at a resolution of 1/8 × 1/8 arc-min (approximately 230 × 230 m) for the open sea, integrated with high-resolution single-beam data collected along cross-shore sections (2–20 m in depth) along the entire coastal area and provided by *Autorità di Sistema Portuale del Mar Tirreno Centro Settentrionale*. The vertical

discretization is based on the z-layers approach. The vertical spacing is 1 m until 15 m below the sea surface, and the resolution then increases progressively (stepwise) to the bottom, reaching a maximum layer thickness of 20 m. This resolution is appropriate for resolving the field in near-river, coastal, and open-sea areas.

Two horizontal configurations have been developed to reproduce coastal dynamics at the river–ocean interface in the Tiber delta zone. The coastal–ocean (CO) configuration (Fig. 2a) covers the two river branches until a few meters from their mouths, with a maximum resolution of 10 m in the southern and northern river branches. The river–coastal–ocean (RCO) configuration (Fig. 2b) is the same as CO, but also includes narrower sections of the two river branches where the grid resolution is less than 10 m. Here, the bathymetry is reconstructed using high-resolution single-beam data corresponding with some cross-river sections and those described in Section 2merged with a morphology dataset extracted from the TINITALY DEM database (Tarquini et al., 2007) at a resolution of 10 m. The resultant bathymetry and topography are illustrated in Fig. 2*a*.

Investigation of the capacity of these two configurations to reproduce near-river dynamics is presented in Section 3.3.

3.2. Forcings and boundary conditions

3.2.1. Atmospheric forcing and surface boundary conditions

For atmospheric fields, the well-consolidated products from the European Centre for Medium-Range Weather Forecasts (ECMWF) (0.1° resolution and 6 h frequency) are adopted as forcings. The atmospheric variables used for parametrization are 2 m air temperature (T2M), 2 m dew point temperature (D2M), total cloud cover (TCC), mean sea level atmospheric pressure (MSL), meridional and zonal 10 m wind components (U10M and V10M, respectively), and total precipitation (TP). The basic surface boundary conditions are as follows. For temperature, air–sea heat flux is parameterized using the bulk formulas described in Pettenuzzo et al. (2010) to calculate net longwave radiation (Bignami et al., 1995), sensible heat (Kondo, 1975), latent heat (Kondo, 1975), evaporation (Kondo, 1975), shortwave solar radiation (Reed, 1977), and solar penetration (Jerlov, 1976). For momentum, surface stress is computed from the wind drag coefficient according to the method of Hellerman and Rosenstein (1983).

3.2.2. Initial and lateral open-ocean boundary conditions

The modeling systems are three-dimensionally downscaled from Med-PHY NRT in terms of both initialization and the open boundaries.

Clamped-type open boundary conditions were employed at the boundary for sea level and inflow tracers, while a zero-gradient boundary condition was used for outflow tracers. Three-dimensional (3D) velocities were adjusted using a relaxation time of 3600 s at the open boundaries.

3.2.3. River forcing

River discharge data were collected at the Ripetta water gauge (provided by Lazio Regional Department of Civil Protection), which is located approximately 40 km from the mouth in the urban area of Rome. Fig. 3 shows the discharges both in terms of hourly values for different years (from 2018 to 2021) and of monthly climatology over the 2005–2021 period.

The monthly climatology of discharge starts to increase from November (maximum value in February of approximately 320 m^3/s) and then decrease significantly starting in May, with minimum values reached in the summer period (approximately 175 m^3/s in August). Although this trend was confirmed by intense flood events in the late autumn and winter of 2020 and 2021, the highest discharge peaks of 2018 and 2019 also aligned with this trend, occurring in March and November, respectively.

The river discharge data at Ripetta described here are imposed on the model domain as a clamped-type lateral open boundary condition. The temperature at these boundaries is set as a zero-gradient boundary condition. Salinity is set to a prescribed value of 0 in the RCO configuration, as we assume that no saline water impacts the upstream portion of the river, and 15 for the CO configuration, as mixed saline and freshwater conditions are found near the river mouths. These values were selected in accordance with sensitivity tests conducted with the Med-PHY NRT parent model and the results of sensitivity tests performed by Simoncelli et al. (2011) based on salinity profiles measured in shelf areas near the river outlets.

3.3. Horizontal domain configurations: coastal–ocean vs. river–coastal–ocean representation

The main objective of this section is to assess the added value of the RCO continuum model compared to the CO representation. To this end, we performed two sensitivity runs using both grids in summer 2019, when historical near-river CTD data were available, to assess the skill of the CO and RCO configurations to reproduce the temperature and salinity profiles at 10 m depth near the northern river branch mouth (see Fig. 1).

In the RCO configuration, the discharge values are those directly measured at the Ripetta station, while in the CO configuration, it is

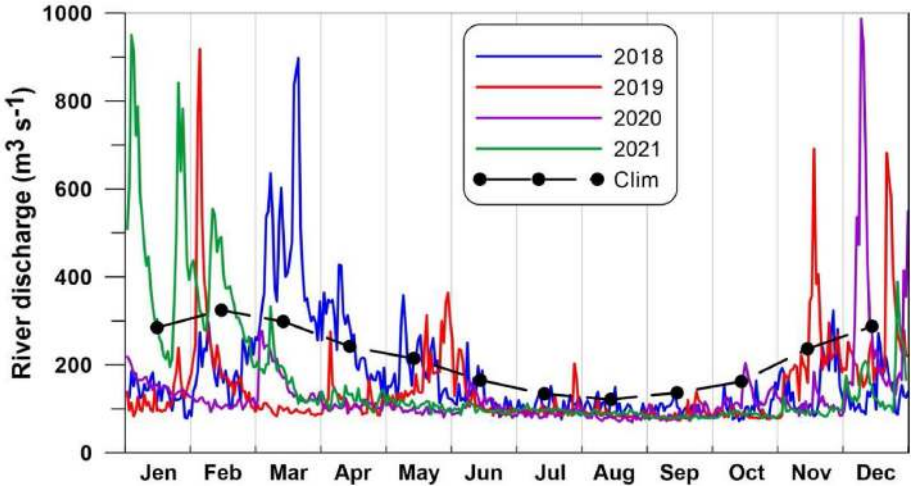

Fig. 3. Tiber River discharge at the Ripetta station. Continuous lines indicate hourly values in each year, while the dashed-dotted line represents monthly climatological values over the 2005–2021 period.

assumed that the southern and northern branches receive approximately 80% and 20% of Tiber runoff, respectively. This partitioning was taken from Mikhailova et al. (1999) and Manca et al. (2014). For both configurations, we assumed that no variation in discharge occurred between the upstream (i.e., the measurement station) and downstream (i.e., before river branches and at river mouths) sections.

The average profiles of temperature and salinity, along with bias and root mean square error (RMSE) values (Fig. 4), demonstrate overall higher accuracy of the RCO configuration, with mean bias values of 0.41 °C and −0.08, compared to 0.54 °C and 0.36 for the CO configuration. Similar skill differences were obtained based on RMSE. The sensitivity experiment indicates very high accuracy for the RCO representation, particularly for the salinity field.

A CO setup could potentially reach the same skill level as RCO, but this achievement would require tuning and calibration over multiple periods for the two key factors: discharge partitioning between the two branches, here set to 20–80% (Mikhailova et al., 1999; Manca et al., 2014), and the prescribed salinity of the mixing salt and fresh waters at the mouths of the two branches, here set to 15 (Oddo et al., 2005; Federico et al., 2017; Verri et al., 2018).

In other words, the RCO configuration minimizes the need for calibration and sensitivity experiments, while still providing good accuracy and skill compared to the observations.

Based on these results, all physical investigations and comparisons presented below were conducted with newly acquired data and the RCO configuration.

4. Validation of the modeling system

The performance of the RCO configuration was evaluated at multiple spatial and temporal scales using CMEMS satellite data and newly acquired observations of temperature, salinity, and sea currents.

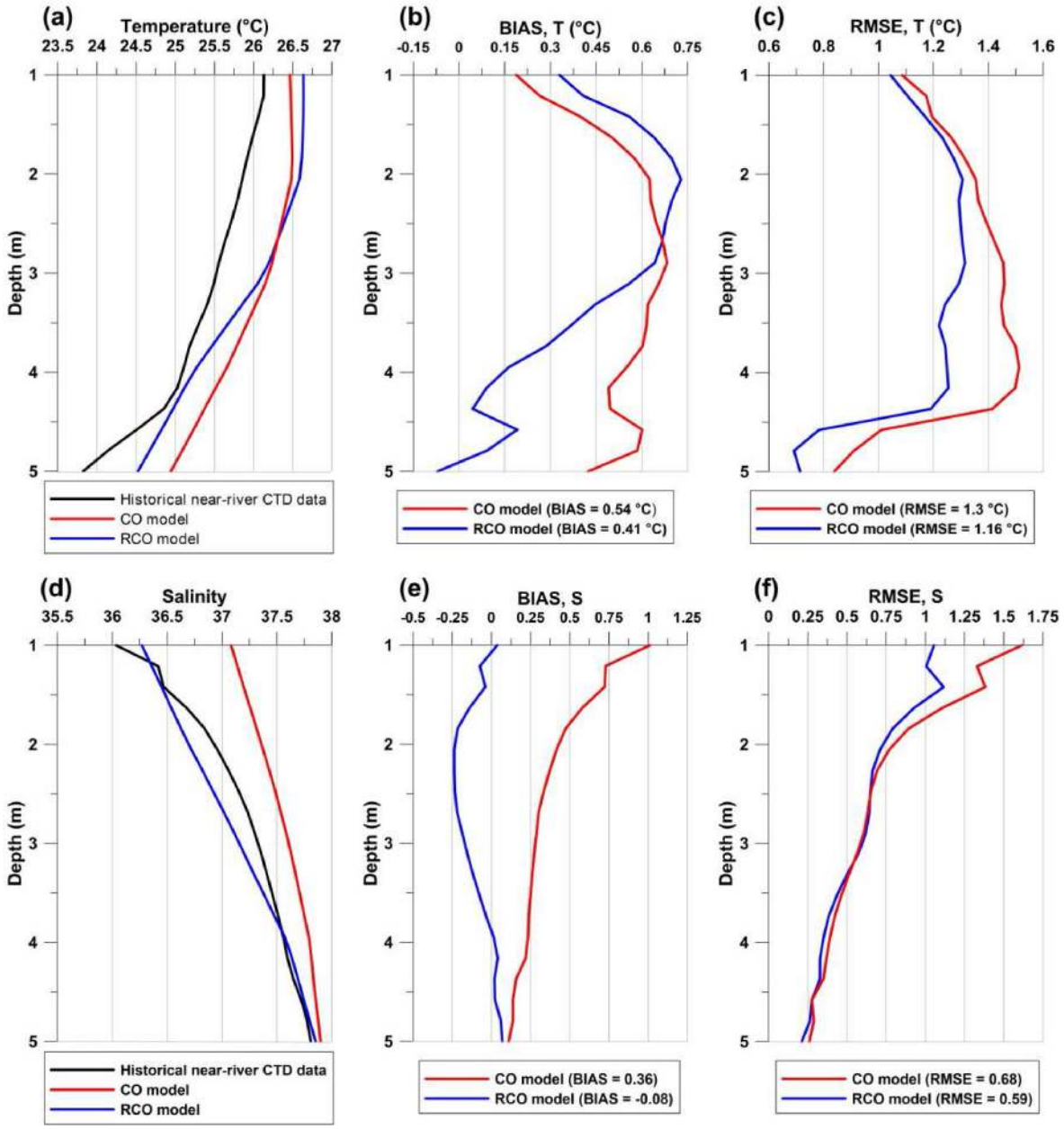

Fig. 4. Validation of the RO and RCO configurations compared to historical near-river CTD data. Average temperature (*a*) and salinity (*d*) profiles with bias (*b, e*) and RMSE (*c, f*) values are shown.

4.1. Offshore ocean scale

The model was run in active mode for 2 years, from January 1, 2018 to December 31, 2019, with 1 month of spin-up (December 2017).

The accuracy of reproducing the mean surface temperature at the offshore scale across the entire study area was analyzed using SST satellite data available from the CMEMS catalog (SST_MED_SST_L4_NRT_OBSERVATIONS_010_004), as illustrated in Fig. 5. In general, the model shows satisfactory skill in simulating mean sea surface temperature variation (mean RMSE = 0.82 °C), with slight overestimation (mean bias = −0.55 °C). The seasonal cycle of SST is apparent, with a mean RMSE in winter of approximately 0.35 °C and higher discrepancies in the spring and summer seasons, reaching a maximum RMSE of 2.7 °C in May 2018 (Fig. 5). These differences are in agreement with the results produced using SHYFEM relative to satellite SST at the regional (e.g., the entire Mediterranean and Black Seas, Barletta et al., 2021) and subregional (e.g., northern Adriatic Sea, McKiver et al., 2016; Turkish Strait System, Ilicak et al., 2021) scales.

Further comparisons were conducted for the offshore CTD profiles. In Fig. 6 we report the average vertical profile of all the offshore CTD stations (indicated by the green dots in Fig. 1). The model provides good accuracy for temperature (RMSE <1.25 °C) and salinity (RMSE <0.11). For the temperature field, the greatest discrepancies appeared in the thermocline zone (bias T = 1.1 °C), which are consistent with values found in other studies employing the same numerical model (Federico et al., 2017; Bajo et al., 2014; Bellafiore et al., 2019; Ferrarin et al., 2019). The greatest differences in salinity profiles occur at the surface (approximately 0.1) and between 10 and 20 m, with a slight vertical shift of the salinity peak.

Fig. 7 shows the annual mean areal distributions of surface temperature, salinity and circulation, while Fig. 8 shows the seasonal mean maps.

The surface temperature field, at both annual and seasonal timescales, shows a well-defined gradient between colder coastal waters and warmer offshore waters. The lowest temperatures occur in the spring in the coastal zones at the northern and southern parts of the study area. Although the water begins to warm during the summer, it reaches its maximum annual values during the autumn.

The surface salinity field is influenced by freshwater discharge from the Tiber River, which affects the northern part of the domain. The maximum extension of the river plume occurs in the spring and summer seasons (reaching approximately 25 km in the north). This timing could be related to the intense flood event in March 2018 (see Fig. 3) and the low intensity of sea currents, which does not favor horizontal mixing of the water masses. By contrast, the high velocity values of the winter and autumn periods lead to limited extension of the plume from the Tiber River, even when intense river discharge occurred in 2019. The different plumes reported in Fig. 8 can be viewed as products of the balance between the tendency toward stratification due to freshwater discharge and the tendency toward homogeneity due to mixing (Kourafalou et al., 1996b*b*).

The surface velocity field is mainly characterized by northward flow in the open ocean. This feature is in accordance with several previous studies (e.g., Artale et al., 1994) and is mainly driven by the presence of a cyclonic eddy sustained by westerly winds through the Bonifacio Strait, which enters at the boundary of our limited-area model from the CMEMS parent model. In the summer season, the direction of the current field changes, becoming less intense due to anticyclonic eddies formed near the coast (Iacono et al., 2021).

In the river–coastal analysis, winter condition exhibits the most prominent near-surface flow toward the coastal areas. This flow is shoreward within the low-salinity zone and is accompanied by a distinct northward current occupying a narrow portion of the nearshore area. This coastal current results from geostrophic adjustment of the flow to the pressure gradient, which occurs primarily due to the density difference between the riverine and ambient waters. In summer, flow in the upper layer is maintained within the bulge of the plume and has a strong offshore component near the mouth, which gradually weakens and turns shoreward at the outer part of the bulge. The low-salinity water that is released by the river is thus first advected offshore, and then deflected to the right and back toward the coast due to the Coriolis force. The resulting onshore flow leads toa zone of low-salinity waters immediately north of the river mouth.

The zone of low-salinity water near the northern branch mouth of the

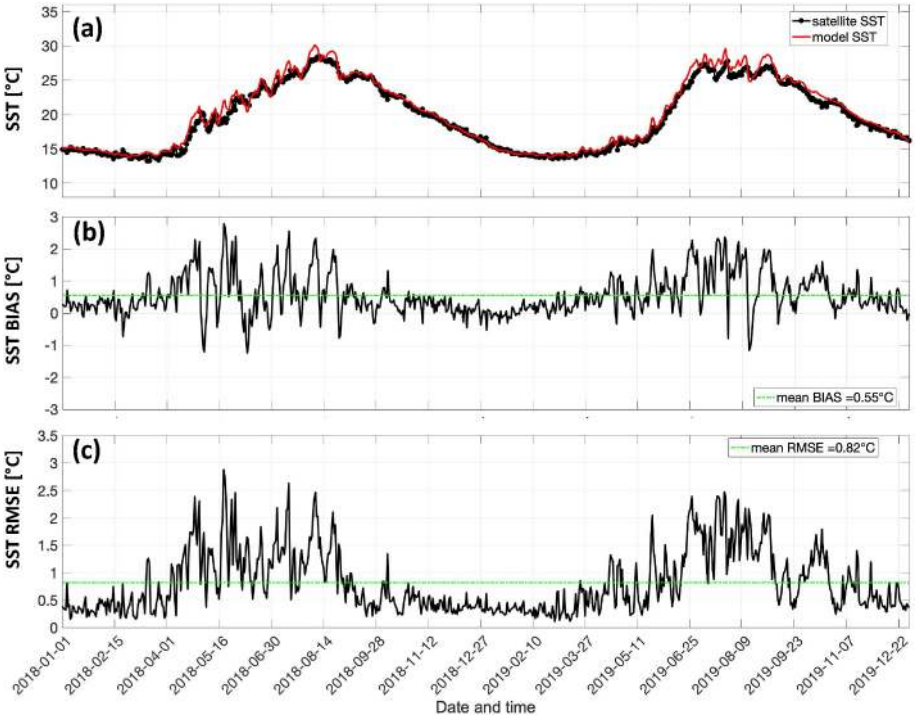

Fig. 5. Comparison between model and satellite temperatures averaged across the entire domain (*a*). The metrics of bias (*b*) and RMSE (*c*) are shown.

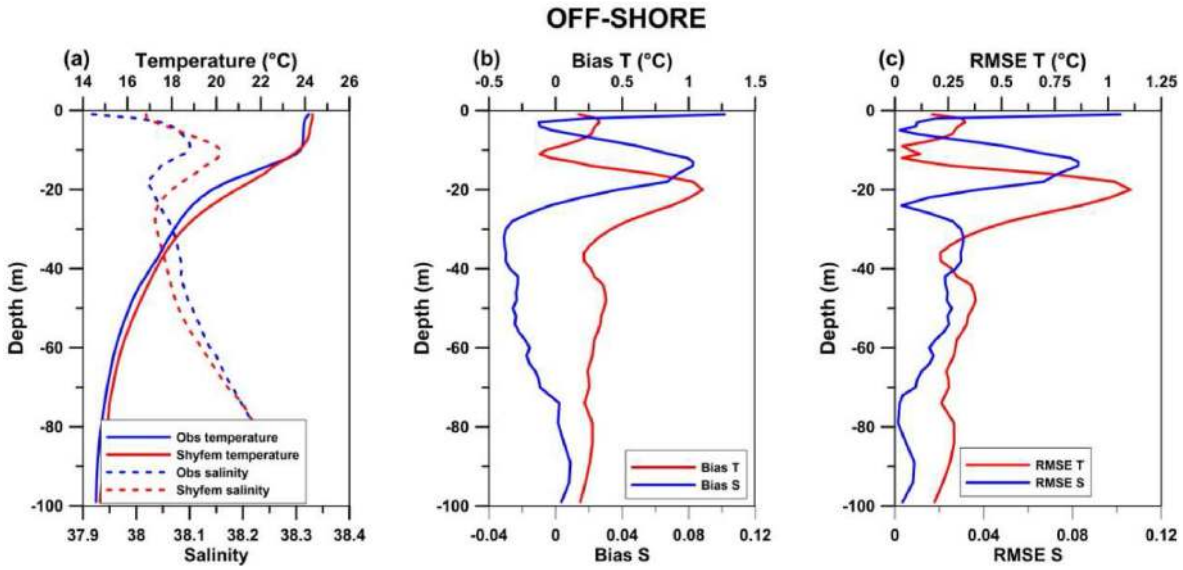

Fig. 6. Model validation compared to offshore CTD casts (indicated by the green dots in Fig. 1) in terms of mean temperature and salinity profile (*a*). The metrics of bias (*b*) and RMSE (*c*) are shown. (For interpretation of the references to colour in this figure legend, the reader is referred to the Web version of this article.)

Tiber River indicates the presence of an anticyclonic gyre (evident in Fig. 7*c*) that is clearly visible in summer, limited in size in spring and autumn and disappears in the winter season. The main drivers of the anticyclonic gyre are discussed in section 5, giving more insights about the role played by the different forcing in the coastal dynamic processes of the Tiber River delta.

4.2. Coastal, near-river and along-river scales

At the coastal, near-river and along-river scales, the model was compared to the newly acquired observational dataset collected to analyze the temperature and salinity of the water column and surface marine currents.

Fig. 9 shows the accuracy of the model compared to CTD data subdivided into coastal (blue dots in Fig. 1) and near-river (red dots in Fig. 1) stations. The results are reported in terms of average profile for both scales.

In the coastal area (Fig. 9 *a, b, c*), the model reconstructs the vertical variation in temperature and salinity with good accuracy, in accordance with the estimates produced for the offshore zone. Very good agreement is obtained in surface layers, while larger discrepancies occur in deeper layers (RMSE for T = 1.25 °C and RMSE for S = 0.07), where temperature is overestimated, and the modeled salinity is lower than the measured value. This finding confirms that the model correctly reproduces heat exchange at the air–sea interface, while also highlighting a limitation in its ability to replicate vertical processes, consistent with the findings reported by Federico et al. (2017). Although model performance decreases in surface layers near the river mouths (Fig. 9) compared to the coastal stations, the results achieved in this portion of the domain could be considered satisfactory for reproducing the complex dynamic processes occurring in the delta coastal zone, which is characterized by the strong salinity gradient and high variability typical of delta areas.

Fig. 10 compares different coastal X-band surface currents for selected wind-driven extreme events between October 2021 and February 2022.The modeled directions of the events show good agreement with measurements in southward-, northward- and inland-oriented cases. The bias of spatial variability has a range of −0.2 to 0.2 m/s, with greater overestimation in cases with more intense surface currents (e.g., Fig. 10*o*) and slight underestimation at lower current intensity (e.g., Fig. 10*i*). The current intensity exhibits a spatial pattern of a decrease when approaching the coasts and port structures, which was clearly reproduced by the model, in accordance with observed values.

The discrepancy between modeled and measured surface currents appears to be consistent with bias values obtained by other authors for coastal modeling systems in the Western Mediterranean, including the studies of García-León et al. (2022) in Spanish ports and Paladini de Mendoza et al. (2018) in the Gulf of Gaeta in Italy.

The overall period of radar operation (October 2021–February 2022) is investigated in terms of the average fields across the entire radar domain using polar diagrams (Fig. 11) to visualize classes of current intensity and directions of observations compared to model results.

The model reproduces the most frequent direction with good accuracy (345°N), even when it estimates higher speeds, which occurred mainly near the river mouth of the northern branch.

In the southern quadrant of the polar diagram, the model results differ slightly from radar observations, as the most frequent class estimated by the model (170°N) is adjacent to that based on measurements (160°N). Overall, the current directions detected using X-band radar show more variability (i.e., the polar diagram has more classes with frequencies greater than 4%) compared to the results of the model. The model's performance at simulating the surface field velocity can be improved by enhancing the spatial and temporal resolutions of surface and boundary conditions (i.e., wind stress) and considering wave effects on coastal circulation during surge events (Roland et al., 2009; Clementi et al., 2017; Causio et al., 2021), such as those monitored with X-band radar.

Further validation was conducted using drifter observations, identified on the basys of their release sites. The modeled currents were input into a downstream Lagrangian drifting objects model (Jansen et al., 2016), a 2D and 3D particle transport model that integrates the particle advection equation using a fourth-order Runge–Kutta method. In this specific case study, the Lagrangian model is configured to simulate surface drift employing currents from the uppermost model layer. Fig. 12 depicts the mean trajectories of six groups of drifters released between February 17 and March 3, 2021, near the two river mouths for the initial 8 h after their release.

The agreement between observed and simulated drifter trajectories is evaluated through the Root Mean Square Error (RMSE), calculated based on the separation distance between the observed and simulated trajectories over simulation time (De Dominicis et al., 2013). The model

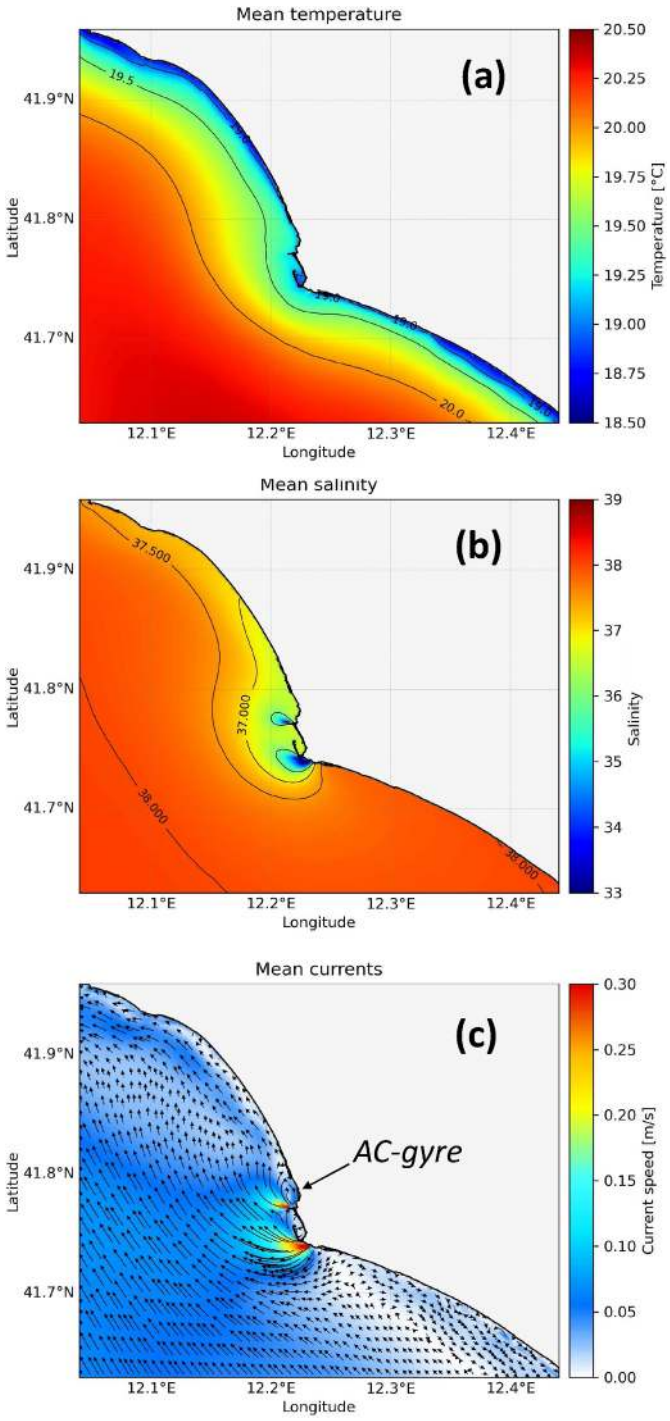

Fig. 7. Annual mean maps of surface temperature (*a*), salinity (*b*), and circulation (*c*). AC-gyre indicates the anticyclonic coastal vortex at the mouth of the northern branch of the Tiber River. The main drivers of gyre formation are discussed in Section 5.

demonstrates the highest accuracy in reproducing the trajectories of three drifters (orange, blue, and green in Fig. 12) released near the northern branch mouth, with an RMSE of approximately 560 m over the average distance covered by these drifters (~6230 m). Near the mouth of the southern branch of the Tiber, the model's performance in simulating the surface current field improves with increasing distance from the river mouth. For the two drifters farthest from the delta (violet and brown in Fig. 12), the average RMSE is about 970 m, calculated over a mean distance traveled of ~9010 m. In contrast, the drifter released at the river mouth (red in Fig. 12) has an RMSE of approximately 1890 m, covering a total distance of ~8970 m. As observed in the comparison with X-band radar data, discrepancies between modeled and observed data may stem from the low spatial and temporal variabilities of the wind forcing and the absence of wave effects on coastal circulation. Notably, forecasting objects floating at sea can be improved using ensemble methods (Vieira et al., 2020).

To assess the capacity of the model to reproduce saltwater intrusion in the southern branch of the Tiber River, the model was compared to salinity values observed during the along-river survey (see Fig. 1*b*) in the spring (May 15, 2022). Fig. 13 shows the along-river salinity section for the southern branch of the Tiber River.

Typical estuarine dynamics (Valle-Levinson, 2010; Ferrarin et al., 2019) can be observed in the Tiber River, with freshwater floating atop denser seawater that moves upstream along the bottom, forming a wedge layer. The model correctly reproduces the horizontal and vertical salinity gradients from the sea (stations 15–17) to upstream station 3. By employing a threshold value of 2 (representing the salinity limit for irrigation) to distinguish between fresh and salt waters, the modeled surface isoline extends approximately 1 km downstream beyond the observed line. Conversely, at the bottom, the modeled isoline reaches 0, whereas the observed line remains higher. This discrepancy is attributed to the fixed boundary condition of 0 imposed along vertical section 1. In other words, the present RCO implementation, designed to allow salt-wedge intrusion up to a limit of 8.8 km upstream, requires upstream extension of the domain, at least for the spring conditions simulated here. The results could be considered acceptable at this stage and are promising in view of future improvements, such as increased vertical resolution by means of generalized tilted time-dependent vertical discretization (Verri et al., 2023).

5. Main drivers of the near-river anti-cyclonic gyre

After successful validation at coastal, near-river and along-river scales, the model was employed to gain insights into coastal hydrodynamics, specifically focusing on phenomena such as the anti-cyclonic gyre highlighted in Fig. 7, which is visible in the northern part of the northern branch of the Tiber River delta.

An Okubo-Weiss (OW) analysis was conducted to investigate the main factors influencing the formation of this gyre. The OW analysis enables the separation of flow into vorticity-dominated and deformation-dominated regions (Isern-Fontanet et al., 2004). In the delta coastal region where the gyre was observed, weekly mean surface velocities for the period between 2018 and 2019 were used to calculate the Okubo-Weiss parameter (OW). OW is positive in strain-dominated regions, while it is negative when the relative vorticity component of the flow prevails. As depicted in Fig. 14*a*, the gyre is present from late spring through early autumn (the blue-shaded area on the graph), consistent with the findings in Fig. 8, where the presence of this anti-cyclonic structure is primarily noted during the summer seasonally-averaged circulation map (Fig. 8*l*).

Given the limited tidal range of the study area (Inghilesi et al., 2012), the sub-tidal circulation resulting from river runoff and wind-induced currents mainly contributes to river delta dynamics (Baldoni et al., 2022) and, consequently, to the formation of the gyre. This assumption finds support in the positive correlation between the Okubo-Weiss parameter and both the Tiber river discharge ($r = 0.59$) and the average wind speed in the area of interest ($r = 0.60$) (Fig. 14b and c). In detail, wind speeds exceeding 2.75 m/s (dotted line of Fig. 2b) and river discharge greater than 235 m^3/s (dotted line of Fig. 2c) consistently inhibit the formation of the anticlockwise gyre.

To further investigate the effect of these driving forces on the formation of the anti-cyclonic gyre, a series of idealized runs were performed with constant and uniformly-distributed river runoff and winds from different directions. These numerical experiments were based on ECMWF wind data and river discharge measurements from the Ripetta

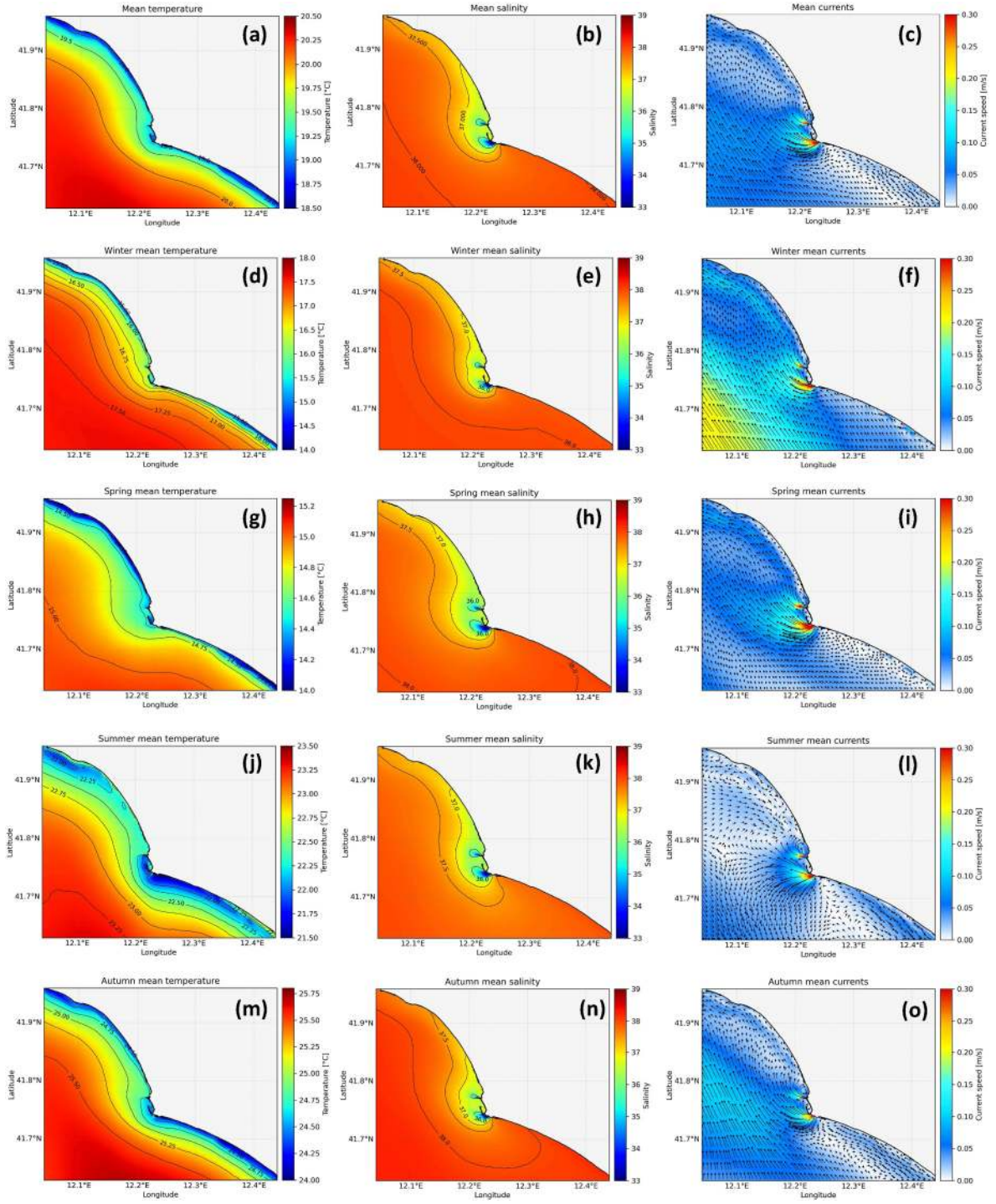

Fig. 8. Annual (*a-c*) and seasonally (*d-o*) averaged maps of sea surface temperature, salinity, and circulation. The seasonal averages were calculated over December–January–February for winter, March–April–May for spring, June–July–August for summer, and September–October–November for autumn.

water gauge, both used as inputs for the RCO configuration of the SHYFEM model.

As detailed in Table 1, we specifically chose three wind direction classes (N, W, and S) capable of triggering gyre formation through interactions with coastal morphology and river runoff. Seaward winds transporting riverine freshwater to the offshore zone (Inghilesi et al., 2012) were excluded. For each of the three directions, we selected river flow and wind velocity intensity corresponding to the 50th percentile (Full-N, Full-W, and Full-S scenarios). To assess the contributions of these driving forces, river forcing was excluded in each of the three simulations to highlight the wind driver (Wind-N, Wind-W, and Wind-S scenarios). Additionally, we conducted an idealized run where wind forcing was excluded to highlight the river driver (River scenario). Each simulation lasted for three days, and the resulting surface velocity field (depicted in Fig. 15) represents the average on the third day.

The gyre becomes apparent when wind-driven currents from the southern and western sectors push the river plume towards the coastline (Full-S and Full-W), leading to a downwelling process that confines the river's freshwater to the coastal area (refer to Fig. 7*b*). When the wind comes from the northern quadrants (Full-N), it generates an along-shore

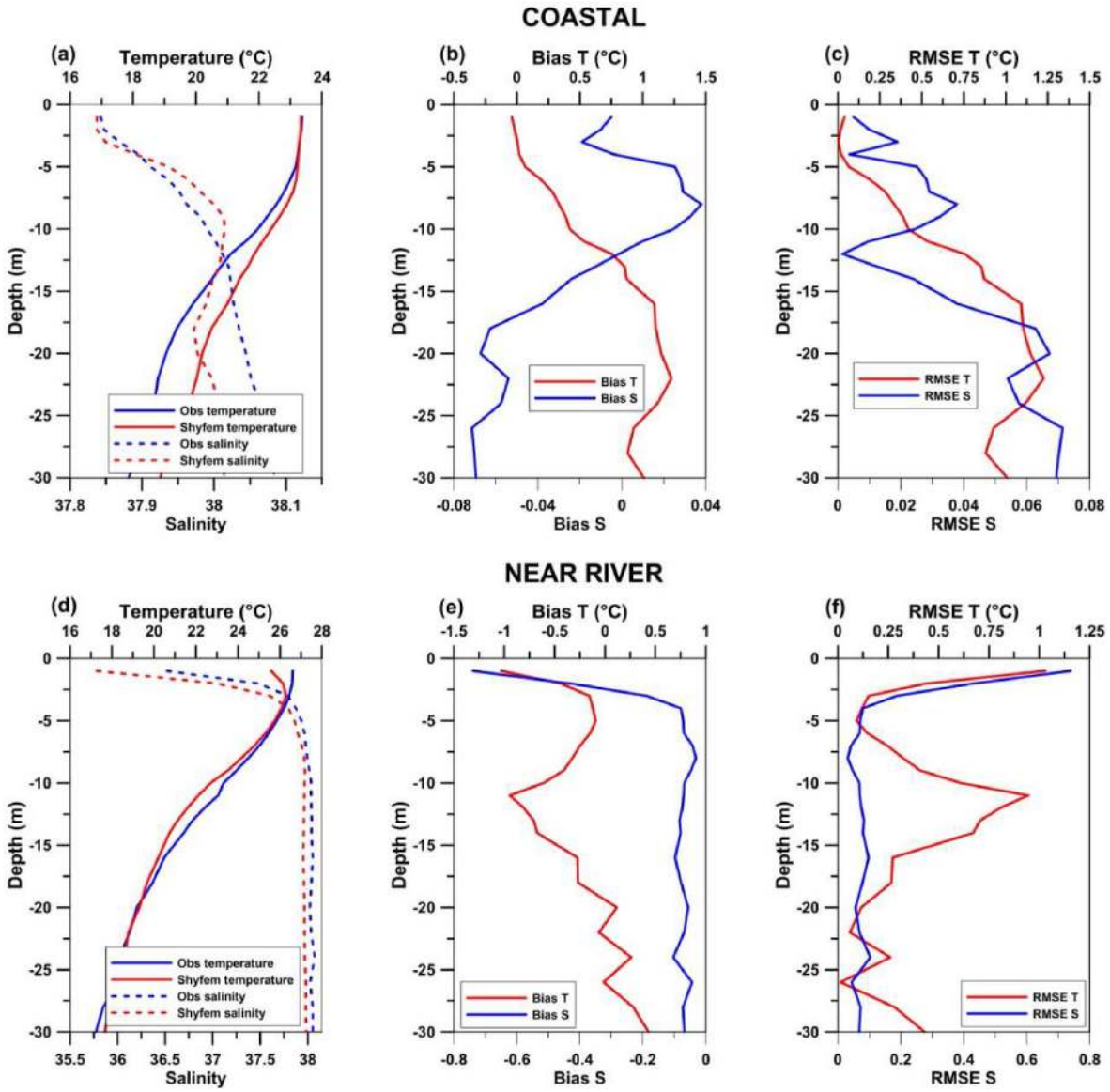

Fig. 9. Model validation through comparison with coastal (*a, b, c*) and near-river (*d, e, f*) CTD data indicated respectively by blue and red dots of Fig. 1. The panels 9*a* and 9*d* report the temperature and salinity average vertical profiles. (For interpretation of the references to colour in this figure legend, the reader is referred to the Web version of this article.)

current that shifts the plume offshore through cross-shore Ekman transport (Fong and Geyer, 2001). In the absence of river discharge, the gyre only forms when the wind blows from the south (Wind-S). This outcome is influenced by the concave shape of the coastline, which encourages the development of anticyclonic structures (Cosoli et al., 2020). As expected, the gyre is also visible when the circulation field is induced by river runoff (River) (Fig. 15*g*), and the modeled river plumes typically consist of an offshore bulge with a coastal current aligning with the direction of Kelvin wave propagation (Kourafalou et al., 1996b*b*).

In conclusion, when both drivers are considered in the simulation (Fig. 15*a*, *b*, *c*), the anticyclonic gyre exhibits high extension and intensity with northward circulation, whereas it disappears when upwelling-favorable wind moves the plume away from the coast, favouring the offshore removal of freshwater.

6. Conclusions

A multi-scale, unstructured-mesh, fully baroclinic model was used to simulate the hydrodynamics of the Tiber River along a continuum from the upstream reaches of the two river branches to the open ocean.

Such a seamless study would not have been practical with a more traditional structured-mesh model, as it would have required nesting of several models within each other that are downscaled or upscale to the regional or local scales. Instead, using an unstructured mesh allows for an integrated approach wherein the coastal model is the same as the river model and the mesh spatial resolution is finely adapted to the characteristic scales of the phenomena being studied (Le Bars et al., 2016).

We demonstrate that the river–coastal–ocean continuum representation (RCO configuration) reproduces the coastal dynamic processes in the Tiber delta zone better than the classic coastal–ocean representation (CO configuration) and minimizes the need for calibration and sensitivity experiments compared to CO, providing good accuracy and skill relative to temperature and salinity observations. The availability of a large amount of newly acquired data (CTD, drifter, X-band radar), obtained ad-hoc for this work, played a key role in evaluation of the accuracy of the RCO model and all of its components. Thanks to this new observational data, the model was successfully validated in water bodies

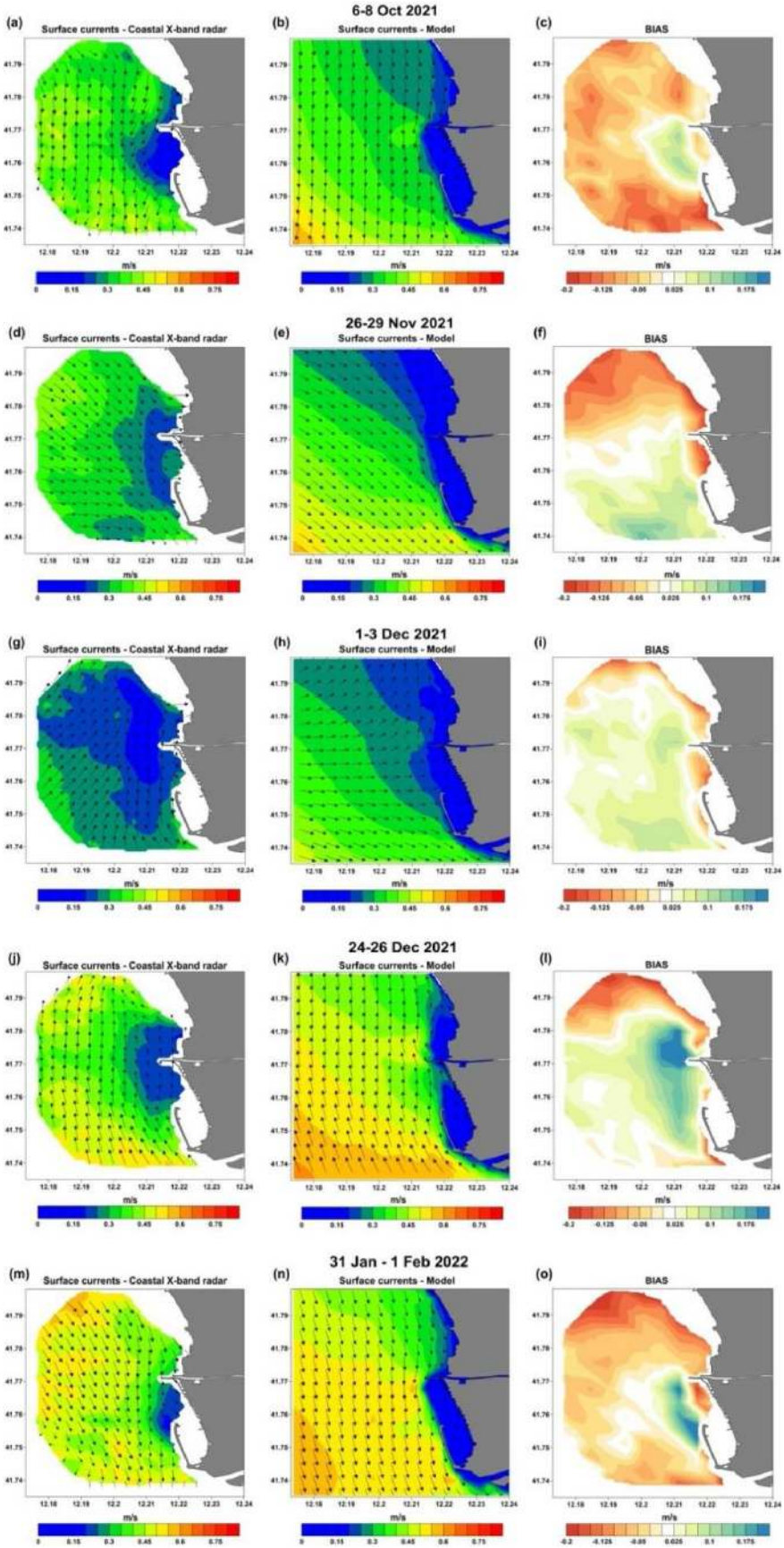

Fig. 10. Surface circulation patterns obtained from coastal X-band radar (*a, d, g, j, m*) and the model (*b, e, h, k, n*) along with bias scores (*c, f, i, l, o*) for five storm events: Oct. 6–8, 2021 (*a, b, c*), Nov. 26–29, 2021 (*d, e, f*), Dec. 4–5, 2021 (*g, h, i*), Dec. 24–26, 2021 (*j, k, l*) and Jan. 31–Feb. 1, 2022 (*m, n, o*).

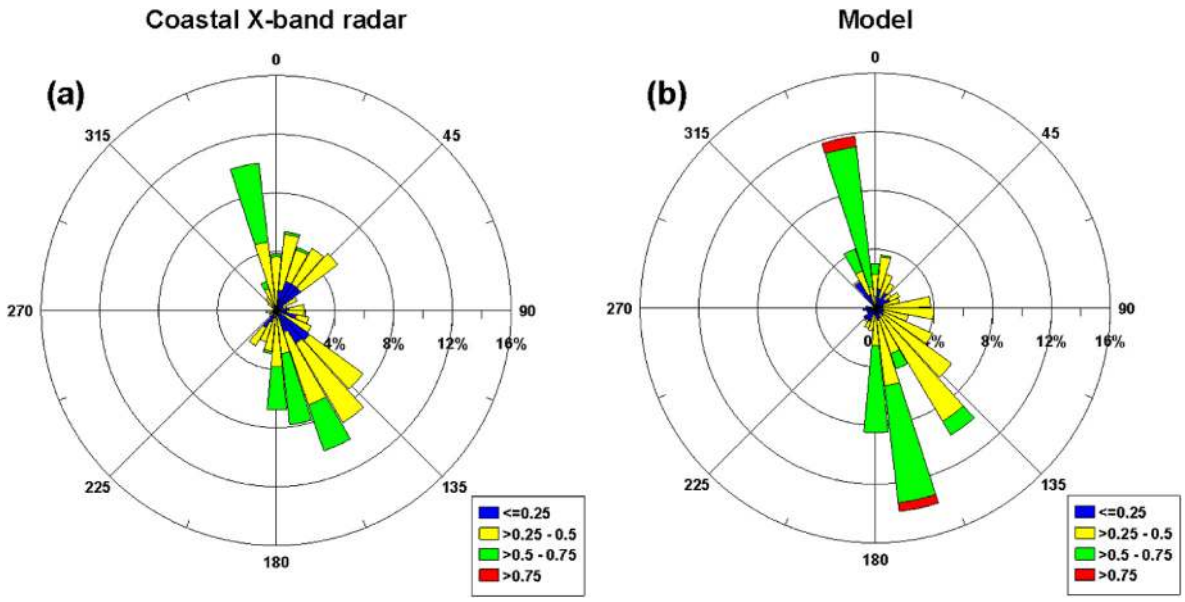

Fig. 11. Polar diagrams of observed and modeled surface currents across the entire spatial domain of the radar observations.

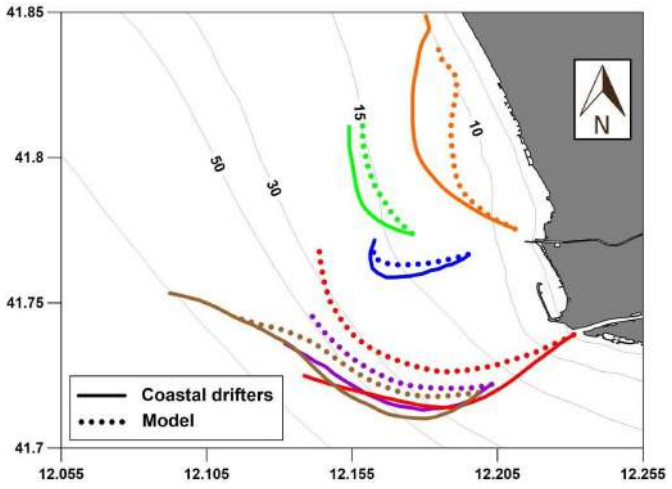

Fig. 12. Drifter trajectories of six drifter groups released in the coastal area (continuous lines) and trajectories simulated with the model (dashed lines).

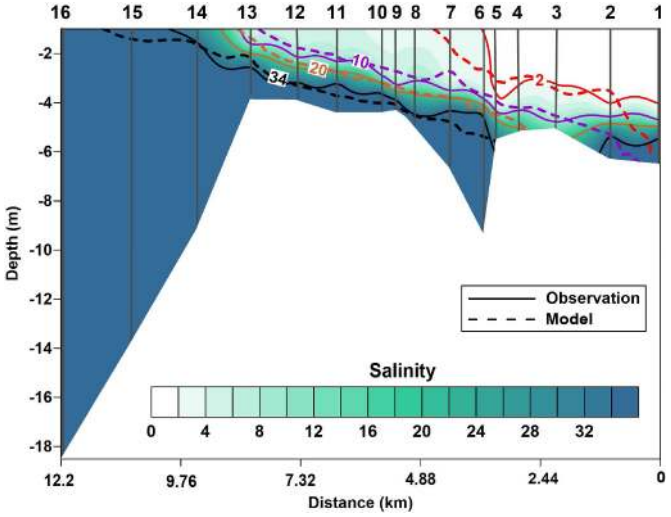

Fig. 13. Along-river salinity section of the southern branch of Tiber River. Colors and continuous contours represent observations, while the dashed lines indicate the modeled values. The salinity section of the model was constructed by averaging data collected on May 15, 2022. (For interpretation of the references to colour in this figure legend, the reader is referred to the Web version of this article.)

covering open-ocean, coastal and estuarine environments and compared against observations of surface currents, salinity, and water temperature at multiple spatial and temporal scales. Nevertheless, performing a comprehensive numerical analysis of specific model components through simplified test cases could provide added value in gaining a deeper understanding of the discrepancies between observed and modeled data.

In general, the model has good accuracy across the offshore, coastal, and near-river scales, reproducing complex dynamic processes occurring in the delta zone, which is characterized by a strong salinity gradient and high variability.

In the future, further validation efforts will be strengthened, particularly in riverine environments, encompassing multiple parameters such as water levels and temperature, in addition to the presented salinity. Moreover, the model's skill at simulating dynamic processes in the coastal zone may increase with novel data assimilation techniques for unstructured meshes (Stefanelli et al., 2022). Furthermore, a limitation of the present study is the analysis of extreme storm surge events. This could be effectively addressed in future studies by advancing the modelling approach to include the effects of waves on hydrodynamics (Roland et al., 2009), enabling a comprehensive interaction between circulation, tides, and waves.

The model can reproduce the salt wedge, providing an estimate of the length of its intrusion and suggesting upstream extension of the domain. Furthermore, the increase in vertical resolution obtained by means of generalized tilted time-dependent vertical discretization (Verri et al., 2023) could further improve the model's capacity to reproduce complex dynamic processes occurring in the delta coastal zone (i.e., river plume dynamics) and within the river branches (i.e., saltwater intrusion).

Finally, the model results suggest the presence of anticyclonic gyre in the vicinity of the river mouth of the northern branch that have not yet been documented. This was made possible by employing an unstructured grid, which, unlike the grid used in other numerical models developed to capture dynamic processes in the Tiber River delta area

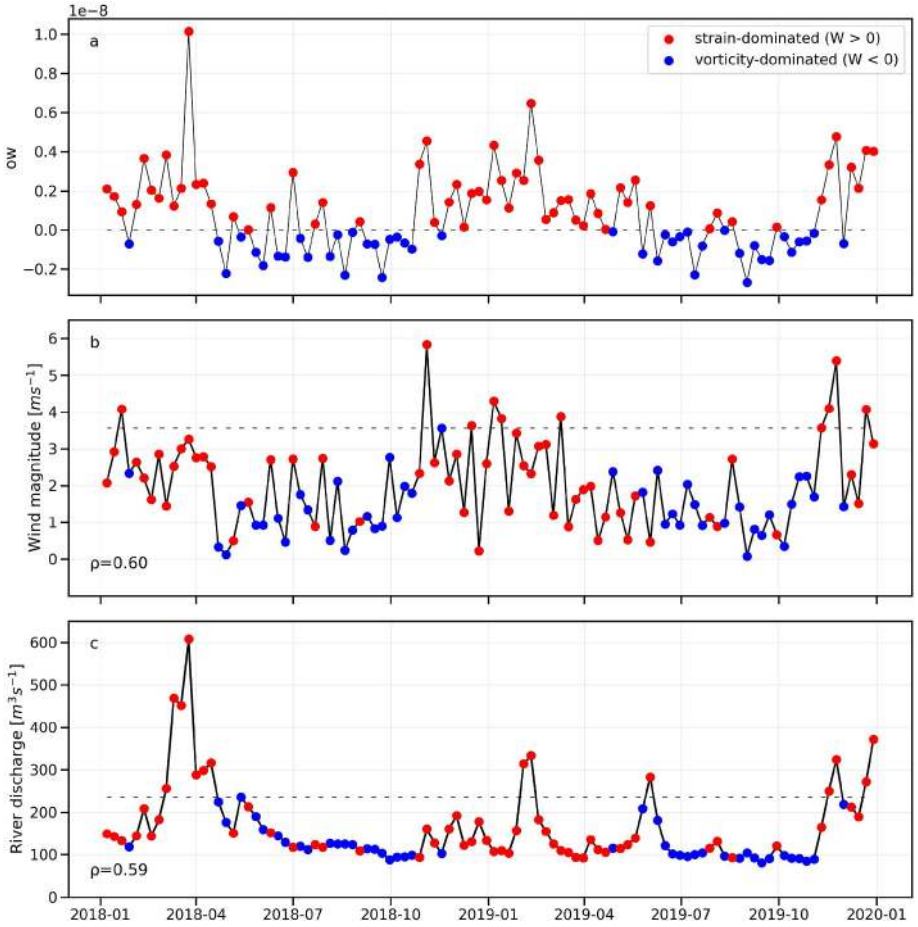

Fig. 14. Okubo-Weiss analysis (*a*) in the area of interest during the period 2018–2019 and comparison with wind speed (*b*) and the river discharge (*c*).

Table 1
Wind (speed and direction) and river discharge values for the idealized scenarios.

Scenario	Wind intensity (m/s)	Wind direction interval (°N)	River discharge (m^3/s)
Full-N	3.0	315–360	125.2
Full-W	3.1	225–270	124.2
Full-S	3.6	135–180	130.3
Wind-N	3.0	315–360	–
Wind-W	3.1	225–270	–
Wind-S	3.6	135–180	–
River	–	–	–

(Inghilesi et al., 2012; Pitarch et al., 2019), enables a detailed analysis of the river-coastal-ocean continuum dynamics. This capability is demonstrated by the identification of gyres near the river mouth in other geographical areas (Le Bars et al., 2016; Maicu et al., 2018). Its presence is due to the contribution of downwelling-favorable wind (southward current direction) and river discharge, as long as their intensities remain below critical thresholds identified through the Okubo-Weiss analysis. These values are associated with subcritical flow conditions (Garvine, 1987; Chao, 1988; Kourafalou et al., 1996b), aligning with the scaling analysis conducted by Inghilesi et al. (2012), which indicates that such conditions occur when the Tiber River's discharge is less than approximately 1000 m^3/s. Values above this threshold occur episodically during the winter season, when northeasterly winds blow seaward in the area of the river mouth, leading to moderate local upwelling and pushing the plume toward the offshore zone (Inghilesi et al., 2012). During the gyre formation period (summer), winds predominantly come from the south and southeast, inducing coastal downwelling conditions that tend to keep the riverine waters close to the shore (Inghilesi et al., 2012). The analysis of the major drivers behind gyre formation through idealized scenarios revealed that events from the south can trigger the formation of the anti-cyclonic structure even in the absence of river runoff. This demonstrates that coastal circulation in the study area is governed by Ekman dynamics (Fong and Geyer, 2001), which results in either upwelling or downwelling depending on the direction of along-shore winds. However, as showed in other studies (Le Bars et al., 2016; Maicu et al., 2018), river flow plays a fundamental role in gyre formation, as it has the capability to generate coastal structures near the river delta even with varying river runoff and limited wind forcing.

Validating the anticyclonic gyre with observational data faced two main challenges: (i) the Lagrangian buoy, deployed at the mouth of the northern branch (Fig. 12, orange line), failed to detect the entire gyre structure, tracing only its border before shifting northward; (ii) the X-band radar domain only partially covered the region where the gyre was observed.

We tried to establish a comprehensive foundation of knowledge through an in-depth examination of the dynamic processes in Tiber river delta area, spanning from the upstream reaches of the two river branches to the open ocean and encompassing the assessment of various contributing factors. This knowledge base will prove invaluable for any forthcoming investigations into the physical and biological processes within this system. These findings are of broad relevance, underscoring the importance of employing high-resolution numerical models, such as the one introduced here, for the study of deltas and estuarine systems as integral components of the river-coastal-ocean continuum.

Finally, given the good performance of the model developed in this study and the continuous acquisition of data in oceanic, coastal, and

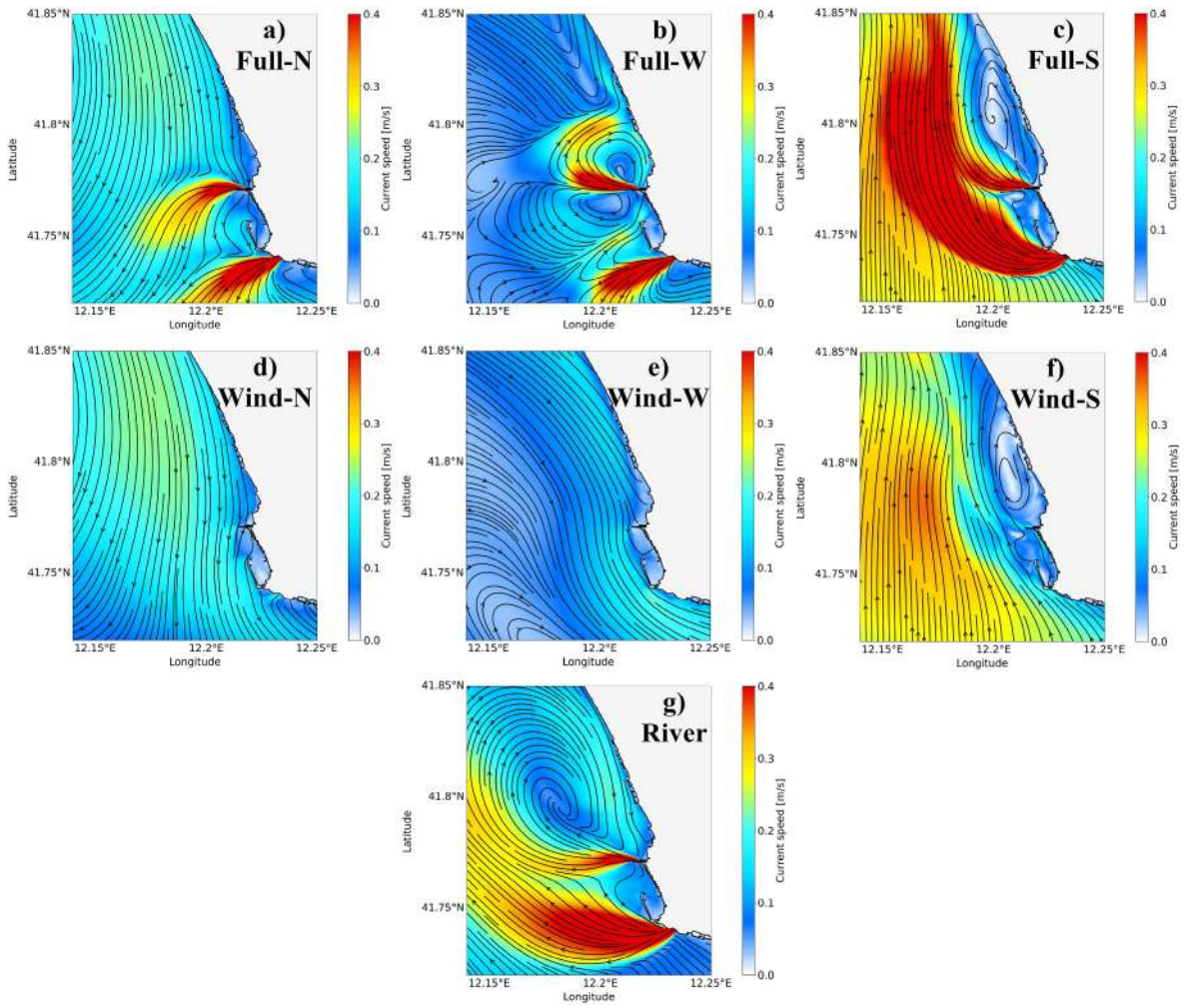

Fig. 15. Drivers of anti-cyclonic gyre formation in the northern branch of Tiber River analyzed by seven idealized scenarios imposing certain river discharge and/or wind speed and direction. (*a*), (*b*) and (*c*) involve both river runoff and wind coming from north, west and south sectors; (*d*), (*e*) and (*f*) exclude the river discharge at the aforementioned scenarios; (*g*) exclusively considers only the effect of the plume on the surface marine current circulation.

riverine waters in the Tiber delta zone, as well as the use of innovative instrumentation (e.g., glider or USV- unmanned surface vehicle), this model can be implemented in the near future within an operational system to support coastal forecasting activities and thus deliver useful and reliable marine condition estimates in the Mediterranean Sea (Kourafalou et al., 2015a; Tintoré et al., 2019).

CRediT authorship contribution statement

Simone Bonamano: Writing – original draft, Visualization, Validation, Software, Methodology, Investigation, Formal analysis, Data curation, Conceptualization. **Ivan Federico:** Writing – review & editing, Writing – original draft, Visualization, Validation, Software, Methodology, Investigation, Conceptualization. **Salvatore Causio:** Writing – review & editing, Visualization, Validation, Software, Investigation. **Viviana Piermattei:** Investigation, Data curation. **Daniele Piazzolla:** Investigation, Data curation. **Sergio Scanu:** Investigation, Data curation. **Alice Madonia:** Investigation, Data curation. **Nicola Madonia:** Validation, Software, Data curation. **Giovanni De Cillis:** Visualization, Software. **Eric Jansen:** Visualization, Software. **Giorgio Fersini:** Resources. **Giovanni Coppini:** Writing – review & editing, Supervision, Software, Investigation, Funding acquisition. **Marco Marcelli:** Writing – review & editing, Supervision, Resources, Project administration, Investigation, Data curation.

Declaration of competing interest

The authors declare that they have no known competing financial interests or personal relationships that could have appeared to influence the work reported in this paper.

Data availability

Data will be made available on request.

Acknowledgments

The research activities described in this study were funded by Autorità di Sistema Portuale del Mar Tirreno Centro Settentrionale within the “Caratterizzazione morfodinamica e di trasporto solido, idrodinamica ed ecologica dell’unità fisiografica Capo Linaro–Capo d’Anzio” project. Simone Bonamano acknowledges the PON Research and Innovation 2014–2020 (European Union–FSE-REACT-EU; contract number 35-G-12752–4) for funding and supporting this research.

References

Alessandri, J., Pinardi, N., Federico, I., Valentini, A., 2023. Storm surge ensemble prediction system for Lagoons and transitional environments. Weather Forecast. 38 (9), 1791–1806. https://doi.org/10.1175/WAF-D-23-0040.1.

Artale, V., Astraldi, M., Buffoni, G., Gasparini, G.P., 1994. Seasonal variability of gyre-scale circulation in the northern Tyrrhenian Sea. J. Geophys. Res. 99, 14127–14137. https://doi.org/10.1029/94JC00284.

Bajo, M., Ferrarin, C., Dinu, I., Umgiesser, G., Stanica, A., 2014. The water circulation near the Danube Delta and the Romanian coast modelled with finite elements. Continent. Shelf Res. 78, 62–74. https://doi.org/10.1016/j.csr.2014.02.006.

Baldoni, A., Perugini, E., Penna, P., Parlagreco, L., Brocchini, M., 2022. A comprehensive study of the river plume in a microtidal setting. Estuar. Coast Shelf Sci. 275, 107995 https://doi.org/10.1016/j.ecss.2022.107995.

Barletta, I., 2021. Seamless Modelling of the Southern European Seas with an Optimized MPI-Based Unstructured-Grid Model. PhD Thesis. Alma Mater Studiorum–Università di Bologna.

Bellafiore, D., Ferrarin, C., Braga, F., Zaggia, L., Maicu, F., Lorenzetti, G., Manfè, G., Brando, V., De Pascalis, F., 2019. Coastal mixing in multiple-mouth deltas: a case study in the Po delta, Italy. Estuarine. Coastal and Shelf Science 226, 106254. https://doi.org/10.1016/j.ecss.2019.106254.

Bignami, F., Marullo, S., Santoleri, R., Schiano, M.E., 1995. Longwave radiation budget in the Mediterranean Sea. J. Geophys. Res.: Oceans 100 (C2), 2501–2514.

Bonamano, S., Piermattei, V., Madonia, A., Paladini de Mendoza, F., Pierattini, A., Martellucci, R., Stefanì, C., Zappalà, G., Caruso, G., Marcelli, M., 2016. The Civitavecchia Coastal Environment Monitoring System (C-CEMS): a new tool to analyze the conflicts between coastal pressures and sensitivity areas. Ocean Sci. 12 (1), 87–100. https://doi.org/10.5194/os-12-87-2016.

Bonamano, S., Piazzolla, D., Scanu, S., Mancini, E., Madonia, A., Piermattei, V., Marcelli, M., 2021. Modelling approach for the evaluation of burial and erosion processes on *Posidonia oceanica* meadows. Estuar. Coast Shelf Sci. 254, 107321 https://doi.org/10.1016/j.ecss.2021.107321.

Buongiorno Nardelli, B., Tronconi, C., Pisano, A., Santoleri, R., 2013. High and ultra-high resolution processing of satellite sea surface temperature data over southern European seas in the framework of MyOcean project. Rem. Sens. Environ. 129, 1–16. https://doi.org/10.1016/j.rse.2012.10.012.

Burchard, H., Petersen, O., 1999. Models of turbulence in the marine environment: a comparative study of two-equation turbulence models. J. Mar. Syst. 21 (1–4), 29–53. https://doi.org/10.1016/S0924-7963(99)00004-4.

Capelli, G., Mazza, R., Papiccio, C., 2007. Saline intrusion in the Tiber Delta. Geology, hydrology and hydrogeology of the coastal plain of the roman sector. Giornale di Geologa Applicata 5, 13–28.

Casulli, V., Cattani, E., 1994. Stability, accuracy and efficiency of a semi-implicit method for three-dimensional shallow water flow. Comput. Math. Appl. 27 (4), 99–112. https://doi.org/10.1016/0898-1221(94)90059-0.

Causio, S., Ciliberti, S.A., Clementi, E., Coppini, G., Lionello, P., 2021. A modelling approach for the assessment of wave-currents interaction in the Black Sea. J. Mar. Sci. Eng. 9 (8), 893. https://doi.org/10.3390/jmse9080893.

Cerralbo, P., Grifoll, M., Valle-Levinson, A., Espino, M., 2014. Tidal transformation and resonance in a short, microtidal Mediterranean estuary (Alfacs Bay in Ebre delta). Estuarine. Coastal and Shelf Science 145, 57–68. https://doi.org/10.1016/j.ecss.2014.04.020.

Chao, S.Y., 1988. Wind-driven motion of estuarine plumes. J. Phys. Oceanogr. 18, 1–23. https://doi.org/10.1175/1520-0485(1988)018<1144:WDMOEP>2.0.CO;2.

Clementi, E., Oddo, P., Drudi, M., Pinardi, N., Korres, G., Grandi, A., 2017. Coupling hydrodynamic and wave models: first step and sensitivity experiments in the Mediterranean Sea. Ocean Dynam. 67 (10), 1293–1312. https://doi.org/10.1007/s10236-017-1087-7.

Clementi, E., Pistoia, J., Escudier, R., Delrosso, D., Drudi, M., Grandi, A., Lecci, R., Cretí, S., Ciliberti, S., Coppini, G., Masina, S., Pinardi, N., 2019. Mediterranean Sea Analysis and Forecast (CMEMS MEDCurrents EAS5 System, 2017–2020) [Data Set]. Copernicus Monitoring Environment Marine Service (CMEMS). https://doi.org/10.25423/CMCC/MEDSEA_ANALYSIS_FORECAST_PHY_006_013_EAS45.

Cosoli, S., Pattiaratchi, C., Hetzel, Y., 2020. High-frequency radar observations of surface circulation features along the south-western Australian coast. J. Mar. Sci. Eng. 8 (2), 97. https://doi.org/10.3390/jmse8020097.

Cucco, A., Sinerchia, M., Ribotti, A., Olita, A., Fazioli, L., Perilli, A., Sorgente, B., Borghini, M., Schroeder, K., Sorgente, R., 2012. A high-resolution real-time forecasting system for predicting the fate of oil spills in the Strait of Bonifacio (western Mediterranean Sea). Mar. Pollut. Bull. 64 (6), 1186–1200. https://doi.org/10.1016/j.marpolbul.2012.03.019.

Darwish, M.S., Moukalled, F., 2003. TVD schemes for unstructured grids. Int. J. Heat Mass Tran. 46 (4), 599–611. https://doi.org/10.1016/S0017-9310(02)00330-7.

Davies, J.L., 1964. A morphogenic approach to world shorelines. Zeitschrift fur Geomorphologie 8, 127–142.

De Dominicis, M., Pinardi, N., Zodiatis, G., Archetti, R.J.G.M.D., 2013. MEDSLIK-II, a Lagrangian marine surface oil spill model for short-term forecasting–Part 2: numerical simulations and validations. Geosci. Model Dev. (GMD) 6 (6), 1871–1888. https://doi.org/10.5194/gmd-6-1871-2013.

Dobricic, S., Pinardi, N., 2008. An oceanographic three-dimensional variational data assimilation scheme. Ocean Model. 22 (3–4), 89–105. https://doi.org/10.1016/j.ocemod.2008.01.004.

El-Adawy, A., Negm, A.M., Saavedra, O.C., Nadaoka, K., El-Shinnawy, I.A., 2014. Coupled hydrodynamic-water quality model for pollution control scenarios in El-Burullus Lake (Nile Delta, Egypt). Am. J. Environ. Sci. 10 (6), 546–565. https://doi.org/10.3844/ajessp.2014.546.565.

Federico, I., Pinardi, N., Coppini, G., Oddo, P., Lecci, R., Mossa, M., 2017. Coastal ocean forecasting with an unstructured grid model in the southern Adriatic and northern Ionian seas. Nat. Hazards Earth Syst. Sci. 17 (1), 45–59. https://doi.org/10.5194/nhess-17-45-2017.

Ferrarin, C., Umgiesser, G., Roland, A., Bajo, M., De Pascalis, F., Ghezzo, M., Scroccaro, I., 2016. Sediment dynamics and budget in a microtidal lagoon–a numerical investigation. Mar. Geol. 381, 163–174. https://doi.org/10.1016/j.margeo.2016.09.006.

Ferrarin, C., Davolio, S., Bellafiore, D., Ghezzo, M., Maicu, F., Mc Kiver, W., Drofa, O., Umgiesser, G., Bajo, M., De Pascalis, F., Malguzzi, P., Zaggia, M., Lorenzetti, G., Manfè, G., 2019. Cross-scale operational oceanography in the Adriatic Sea. Journal of Operational Oceanography 12 (2), 86–103. https://doi.org/10.1080/1755876X.2019.1576275.

Fofonova, V., Kärnä, T., Klingbeil, K., Androsov, A., Kuznetsov, I., Sidorenko, D., Danilov, S., Burchard, H., Wiltshire, K.H., 2021. Plume spreading test case for coastal ocean models. Geosci. Model Dev. (GMD) 14 (11), 6945–6975. https://doi.org/10.5194/gmd-14-6945-2021.

Fong, D.A., Geyer, W.R., 2001. Response of a river plume during an upwelling favorable wind event. J. Geophys. Res.: Oceans 106 (C1), 1067–1084. https://doi.org/10.1029/2000JC900134.

García-León, M., Sotillo, M.G., Mestres, M., Espino, M., Fanjul, E.Á., 2022. Improving operational ocean models for the Spanish Port authorities: assessment of the Samoa coastal forecasting service upgrades. J. Mar. Sci. Eng. 10 (2), 149. https://doi.org/10.3390/jmse10020149.

Garvine, R.W., 1987. Estuary plumes and fronts in shelf waters: a layer model. J. Phys. Oceanogr. 17, 1877–1896. https://doi.org/10.1175/1520-0485(1987)017<1877:EPAFIS>2.0.CO;2.

Hellerman, S., Rosenstein, M., 1983. Normal monthly wind stress over the world ocean with error estimates. J. Phys. Oceanogr. 13 (7), 1093–1104. https://doi.org/10.1175/1520-0485(1983)013<1093:NMWSOT>2.0.CO;2.

Iacono, R., Napolitano, E., Palma, M., Sannino, G., 2021. The Tyrrhenian Sea circulation: a review of recent work. Sustainability 13 (11), 6371. https://doi.org/10.3390/su13116371.

Ilicak, M., Federico, I., Barletta, I., Mutlu, S., Karan, H., Ciliberti, S.A., Clementi, E., Coppini, G., Pinardi, N., 2021. Modeling of the Turkish strait system using a high-resolution unstructured grid ocean circulation model. J. Mar. Sci. Eng. 9 (7), 769. https://doi.org/10.3390/jmse9070769.

Inghilesi, R., Ottolenghi, L., Orasi, A., Pizzi, C., Bignami, F., Santoleri, R., 2012. Fate of river Tiber discharge investigated through numerical simulation and satellite monitoring. Ocean Sci. 8 (5), 773–786. https://doi.org/10.5194/os-8-773-2012.

Isern-Fontanet, J., Font, J., García-Ladona, E., Emelianov, M., Millot, C., Taupier-Letage, I., 2004. Spatial structure of anticyclonic eddies in the Algerian basin (Mediterranean Sea) analyzed using the Okubo–Weiss parameter. Deep Sea Res. Part II Top. Stud. Oceanogr. 51 (25–26), 3009–3028. https://doi.org/10.1016/j.dsr2.2004.09.013.

Jansen, E., Coppini, G., Pinardi, N., 2016. Drift simulation of MH370 debris using super ensemble techniques. Nat. Hazards Earth Syst. Sci. 16 (7), 1623–1628. https://doi.org/10.5194/nhess-16-1623-2016.

Jerlov, N.G., 1976. Marine Optics. Elsevier, p. 230.

Jickells, T.D., Andrews, J.E., Parkes, D.J., 2016. Direct and indirect effect of estuarine reclamation on nutrient and metal fluxes in the global coastal zone. Aquat. Geochem. 22 (4), 337–348. https://doi.org/10.1007/s10498–015–9278–7.

Kondo, J., 1975. Air-sea bulk transfer coefficients in diabatic conditions. Boundary-Layer Meteorol. 9 (1), 91–112.

Kourafalou, V.H., Lee, T.N., Oey, L.Y., Wang, J.D., 1996a. The fate of river discharge on the continental shelf: 2. Transport of coastal low-salinity waters under realistic wind and tidal forcing. J. Geophys. Res.: Oceans 101 (C2), 3435–3455. https://doi.org/10.1029/95JC03025.

Kourafalou, V.H., Oey, L.Y., Wang, J.D., Lee, T.N., 1996b. The fate of river discharge on the continental shelf: 1. Modeling the river plume and the inner shelf coastal current. J. Geophys. Res.: Oceans 101 (C2), 3415–3434. https://doi.org/10.1029/95JC03024.

Kourafalou, V.H., De Mey, P.D., Le Hénaff, M., Charria, G., Edwards, C.A., He, R., Herzfeld, M., Pascual, A., Stanev, E.V., Tintoré, J., Usui, N., van der Westhuysen, A. J., Wilkin, J., Zhu, X., 2015a. Coastal ocean forecasting: system integration and evaluation. Journal of Operational Oceanography 8 (Suppl. 1), s127–s146. https://doi.org/10.1080/1755876X.2015.1022336.

Kourafalou, V.H., Mey, P.D., Staneva, J., Ayoub, N., Barth, A., Chao, Y., Cirano, M., Fiechter, J., Herzfeld, M., Kurapov, A., Moore, A.M., Oddo, P., Pullen, J., van der Westhuysen, A., Weisberg, R.H., 2015b. Coastal ocean forecasting: Science foundation and user benefits. Journal of Operational Oceanography 8 (Suppl. 1), s147–s167. https://doi.org/10.1080/1755876X.2015.1022348.

La Vigna, F., Ciadamidaro, S., Mazza, R., Mancini, L., 2010. Water quality and relationship between superficial and ground water in Rome (Aniene River basin, central Italy). Environ. Earth Sci. 60 (6), 1267–1279. https://doi.org/10.1007/s12665–009–0267–2.

Le Bars, Y., Vallaeys, V., Deleersnijder, É., Hanert, E., Carrere, L., Channelière, C., 2016. Unstructured-mesh modeling of the Congo river-to-sea continuum. Ocean Dynam. 66 (4), 589–603. https://doi.org/10.1007/s10236-016-0939-x.

Madec, G., 2008. The Nucleus for European modelling of the Ocean team. NEMO ocean engine, Note du Pôle de modélisation. Institut Pierre-Simon Laplace (IPSL), France (27).

Maicu, F., De Pascalis, F., Ferrarin, C., Umgiesser, G., 2018. Hydrodynamics of the Po river-Delta-Sea system. J. Geophys. Res.: Oceans 123 (9), 6349–6372. https://doi.org/10.1029/2017JC013601.

Maicu, F., Alessandri, J., Pinardi, N., Verri, G., Umgiesser, G., Lovo, S., Turolla, S., Paccagnella, T., Valentini, A., 2021. Downscaling with an unstructured coastal-ocean model to the Goro lagoon and the Po River Delta branches. Front. Mar. Sci. 8, 647781 https://doi.org/10.3389/fmars.2021.647781.

Manca, F., Capelli, G., La Vigna, F., Mazza, R., Pascarella, A., 2014. Wind-induced salt-wedge intrusion in the Tiber River mouth (Rome–Central Italy). Environ. Earth Sci. 72 (4), 1083–1095. https://doi.org/10.1007/s12665-013-3024-5.

Marcelli, M., Caburazzi, M., Perilli, A., Piermattei, V., Fresi, E., 2005. Deep chlorophyll maximum distribution in the central Tyrrhenian Sea described by a towed undulating vehicle. Chem. Ecol. 21 (5), 351–367. https://doi.org/10.1080/02757540500290248.

Marcelli, M., Piermattei, V., Gerin, R., Brunetti, F., Pietrosemoli, E., Addo, S., Boudaya, L., Coleman, R., Olubumni, N., Rick, J., Sarker, S., Sohou, Z., Zennaro, M., Wiltshire, K., Crise, A., 2021. Toward the widespread application of low-cost technologies in coastal ocean observing (Internet of Things for the Ocean). Mediterr. Mar. Sci. 22 (2), 255–269. https://doi.org/10.12681/mms.25060.

Martellucci, R., Salon, S., Cossarini, G., Piermattei, V., Marcelli, M., 2021. Coastal phytoplankton bloom dynamics in the Tyrrhenian Sea: advantage of integrating in situ observations, large-scale analysis and forecast systems. J. Mar. Syst. 218, 103528 https://doi.org/10.1016/j.jmarsys.2021.103528.

McKiver, W.J., Sannino, G., Braga, F., Bellafiore, D., 2016. Investigation of model capability in capturing vertical hydrodynamic coastal processes: a case study in the north Adriatic Sea. Ocean Sci. 12 (1), 51–69. https://doi.org/10.5194/os-12-51-2016.

Micaletto, G., Barletta, I., Mocavero, S., Federico, I., Epicoco, I., Verri, G., Coppini, G., Schiano, P., Aloisio, G., Pinardi, N., 2022. Parallel implementation of the SHYFEM (system of HydrodYnamic finite element Modules) model. Geosci. Model Dev. (GMD) 15 (15), 6025–6046. https://doi.org/10.5194/gmd-15-6025-2022.

Mikhailova, M.V., Bellotti, P., Valeri, P., Tortora, P., 1999. Intrusion of seawater into the river part of the Tiber mouth. Water Resour. 26 (6), 679–686.

Oddo, P., Pinardi, N., Zavatarelli, M., 2005. A numerical study of the interannual variability of the Adriatic Sea (2000–2002). Science of theTotal Environment 353, 39–56. https://doi.org/10.1016/j.scitotenv.2005.09.061.

Paladini de Mendoza, F., Bonamano, S., Martellucci, R., Melchiorri, C., Consalvi, N., Piermattei, V., Marcelli, M., 2018. Circulation during storms and dynamics of suspended matter in a sheltered coastal area. Rem. Sens. 10 (4), 602. https://doi.org/10.3390/rs10040602.

Park, K., Federico, I., Di Lorenzo, E., Ezer, T., Cobb, K.M., Pinardi, N., Coppini, G., 2022. The contribution of hurricane remote ocean forcing to storm surge along the southeastern US coast. Coast Eng. 173, 104098 https://doi.org/10.1016/j.coastaleng.2022.104098.

Pettenuzzo, D., Large, W.G., Pinardi, N., 2010. On the corrections of ERA-40 surface flux products consistent with the Mediterranean heat and water budgets and the connection between basin surface total heat flux and NAO. J. Geophys. Res.: Oceans 115 (C6). https://doi.org/10.1029/2009JC005631.

Piermattei, V., Madonia, A., Bonamano, S., Martellucci, R., Bruzzone, G., Ferretti, R., Odetti, A., Azzaro, M., Zappalà, G., Marcelli, M., 2018. Cost-effective technologies to study the arctic ocean environment. Sensors 18 (7), 2257. https://doi.org/10.3390/s18072257.

Pitarch, J., Falcini, F., Nardin, W., Brando, V.E., Di Cicco, A., Marullo, S., 2019. Linking flow-stream variability to grain size distribution of suspended sediment from a satellite-based analysis of the Tiber River plume (Tyrrhenian Sea). Sci. Rep. 9 (1), 1–10. https://doi.org/10.1038/s41598-019-56409-8.

Postacchini, M., Manning, A.J., Calantoni, J., Smith, J.P., Brocchini, M., 2023. A storm driven turbidity maximum in a microtidal estuary. Estuar. Coast Shelf Sci. 288, 108350 https://doi.org/10.1016/j.ecss.2023.108350.

Rasmussen, E.K., Svenstrup Petersen, O., Thompson, J.R., Flower, R.J., Ahmed, M.H., 2009. Hydrodynamic-ecological model analyses of the water quality of Lake Manzala Nile Delta, northern Egypt. Hydrobiologia 622 (1), 195–220. https://doi.org/10.1007/s10750–008–9683–7.

Reed, R., 1977. On estimating insolation over the ocean. J. Phys. Oceanogr. 7, 482–485.

Remacle, J.F., Henrotte, F., Carrier-Baudouin, T., Béchet, E., Marchandise, E., Geuzaine, C., Mouton, T., 2013. A frontal Delaunay quad mesh generator using the L∞ norm. Int. J. Numer. Methods Eng. 94 (5), 494–512. https://doi.org/10.1002/nme.4458.

Ribotti, A., Bussani, A., Menna, M., Satta, A., Sorgente, R., Cucco, A., Gerin, R., 2022. A Mediterranean drifters dataset: 1998–2022. Earth Syst. Sci. Data Discuss. 1–12. https://doi.org/10.5194/essd-2022-344.

Roland, A., Cucco, A., Ferrarin, C., Hsu, T.W., Liau, J.M., Ou, S.H., Umgiesser, G., Zanke, U., 2009. On the development and verification of a 2-D coupled wave-current model on unstructured meshes. J. Mar. Syst. 78, S244–S254. https://doi.org/10.1016/j.jmarsys.2009.01.026.

Schofield, O., Bergmann, T., Bissett, P., Grassle, J.F., Haidvogel, D.B., Kohut, J., Moline, M., Glenn, S.M., 2002. The long-term ecosystem observatory: an integrated coastal observatory. IEEE J. Ocean. Eng. 27, 146–154. https://doi.org/10.1109/JOE.2002.1002469.

Schroeder, K., Gasparini, G.P., Tangherlini, M., Astraldi, M., 2006. Deep and intermediate water in the western Mediterranean under the influence of the Eastern Mediterranean transient. Geophys. Res. Lett. 33 (21) https://doi.org/10.1029/2006GL027121.

Serafino, F., Lugni, C., Soldovieri, F., 2010. A novel strategy for the surface current determination from marine X-band radar data. Geosci. Rem. Sens. Lett. IEEE 7 (2), 231–235. https://doi.org/10.1109/LGRS.2009.2031878.

Simoncelli, S., Pinardi, N., Oddo, P., Mariano, A.J., Montanari, G., Rinaldi, A., Deserti, M., 2011. Coastal rapid environmental assessment in the northern Adriatic Sea. Dynam. Atmos. Oceans 52 (1–2), 250–283. https://doi.org/10.1016/j.dynatmoce.2011.04.004.

Smagorinsky, J., 1963. General circulation experiments with the primitive equations. Mon. Weather Rev. 91, 99–164.

Sorgente, R., Di Maio, A., Pessini, F., Ribotti, A., Bonomo, S., Perilli, A., Alberico, I., Lirer, F., Cascella, A., Ferraro, L., 2020. Impact of freshwater inflow from the Volturno river on coastal circulation. Front. Mar. Sci. 7, 293. https://doi.org/10.3389/fmars.2020.00293.

Stanev, E.V., Grashorn, S., Zhang, Y.J., 2017. Cascading ocean basins: numerical simulations of the circulation and inter basin exchange in the Azov–Black–Marmara-Mediterranean Seas system. Ocean Dynam. 67, 1003–1025. https://doi.org/10.1007/s10236-017-1071-2.

Stefanelli, M., Jansen, E., Aydogdu, A., Federico, I., Coppini, G., Pinardi, N., 2022. Variational data assimilation for advanced cross-scale ocean modelling (No. EGU22–4741). In: Copernicus Meetings.

Storto, A., Masina, S., Navarra, A., 2016. Evaluation of the CMCC eddy-permitting global ocean physical reanalysis system (c-glors, 1982–2012) and its assimilation components. Q. J. R. Meteorol. Soc. 142 (695), 738–758. https://doi.org/10.1002/qj.2673.

Tarquini, S., Isola, I., Favalli, M., Mazzarini, F., Bisson, M., Pareschi, M.T., Boschi, E., 2007. TINITALY/01: a new triangular irregular network of Italy. Ann. Geophys. 50 (3), 407–425.

Tintoré, J., Pinardi, N., Álvarez-Fanjul, E., Aguiar, E., Álvarez-Berastegui, D., Bajo, M., Balbin, R., Bozzano, R., Buongiorno Nardelli, B., Cardin, V., Casas, B., Charcos-Llorens, M., Chiggiato, J., Clementi, E., Coppini, G., Coppola, L., Cossarini, G., Deidun, A., Deudero, S., D'Ortenzio, F., Drago, A., Drudi, M., El Serafy, G., Escudier, R., Farcy, P., Federico, I., Gabriel Fernández, J., Ferrarin, C., Fossi, C., Frangoulis, C., Galgani, F., Gana, S., García Lafuente, J., García Sotillo, M., Garreau, P., Gertman, I., Gómez-Pujol, L., Grandi, A., Hayes, D., Hernández-Lasheras, J., Herut, B., Heslop, E., Hilmi, K., Juza, M., Kallos, G., Korres, G., Lecci, R., Lazzari, P., Lorente, P., Liubartseva, S., Louanchi, F., Malacic, V., Mannarini, G., March, D., Marullo, S., Mauri, E., Meszaros, L., Mourre, B., Mortier, L., Muñoz-Mas, C., Novellino, A., Obaton, D., Orfil, A., Pascual, A., Pensieri, S., Pérez Gómez, B., Pérez Rubio, S., Perivoliotis, L., Petihakis, G., Petit de la Villéon, L., Pistoia, J., Poulain, P.M., Pouliquen, S., Prieto, L., Raimbault, P., Reglero, P., Reyes, E., Rotlan, P., Ruiz, S., Ruiz, J., Ruiz, I., Ruiz-Orejón, L.F., Salihoglu, B., Salon, S., Sammartino, S., Sánchez Arcilla, A., Sánchez-Román, A., Sannino, G., Santoleri, R., Sardà, R., Schroeder, K., Simoncelli, S., Sofianos, S., Sylaios, G., Tanhua, T., Teruzzi, A., Testor, P., Tezcan, D., Torner, M., Trotta, F., Umgiesser, G., von Schuckmann, K., Verri, G., Vilibic, I., Yucel, M., Zavatarelli, M., Zodiatis, G., 2019. Challenges for sustained observing and forecasting systems in the Mediterranean Sea. Front. Mar. Sci. 568, 1–30. https://doi.org/10.3389/fmars.2019.00568.

Trotta, F., Federico, I., Pinardi, N., Coppini, G., Causio, S., Jansen, E., Iovino, D., Masina, S., 2021. A relocatable ocean modeling platform for downscaling to shelf-coastal areas to support disaster risk reduction. Front. Mar. Sci. 8, 642815 https://doi.org/10.3389/fmars.2021.642815.

Umgiesser, G., Canu, D.M., Cucco, A., Solidoro, C., 2004. A finite element model for the Venice Lagoon. Development, set up, calibration and validation. J. Mar. Syst. 51 (1–4), 123–145. https://doi.org/10.1016/j.jmarsys.2004.05.009.

Valle-Levinson, A., 2010. Contemporary Issues in Estuarine Physics. Cambridge University Press, New York, USA.

Verri, G., Pinardi, N., Oddo, P., Ciliberti, S.A., Coppini, G., 2018. River runoff influences on the Central Mediterranean overturning circulation. Clim. Dynam. 50 (5), 1675–1703. https://doi.org/10.1007/s00382-017-3715-9.

Verri, G., Barletta, I., Pinardi, N., Federico, I., Alessandri, J., Coppini, G., 2023. Shelf slope, estuarine dynamics and river plumes in az* vertical coordinate, unstructured grid model. Ocean Model. 102235 https://doi.org/10.1016/j.ocemod.2023.102235.

Vieira, G.S., Rypina, I.I., Allshouse, M.R., 2020. Uncertainty quantification of trajectory clustering applied to ocean ensemble forecasts. Fluid 2020, 184. https://doi.org/10.3390/fluids5040184.

Wilkin, J., Rosenfeld, L., Allen, A., Baltes, R., Baptista, A., He, R., Hogan, P., Kurapov, A., Mehra, A., Quintrell, J., Schwab, D., Signell, R., 2017. Advancing coastal ocean modelling, analysis, and prediction for the US Integrated Ocean Observing System. Journal of Operational Oceanography 10 (2), 115–126. https://doi.org/10.1080/1755876X.2017.1322026.